Preprint 29 May 2025

# A black hole in a near-pristine galaxy 700 million years after the Big Bang

Roberto Maiolino [1,2,3], Hannah Übler [4], Francesco D'Eugenio [1,2], Jan Scholtz [1,2], Ignas Juodžbalis [1,2], Michele Perna [5], Volker Bromm [6,7], Pratika Dayal [8], Sophie Koudmani [1,9,10,11,12], Boyuan Liu [6,10,13], Raffaella Schneider [14,15,16,17], Debora Sijacki [1,10], Rosa Valiante [14,16], Alessandro Trinca [18,15,16], Saiyang Zhang [19,7], Marta Volonteri [20], Kohei Inayoshi [21], Stefano Carniani [22], Kimihiko Nakajima [23], Yuki Isobe [1,2,24], Joris Witstok [25,26], Gareth C. Jones [1,2], Sandro Tacchella [1,2], Santiago Arribas [5], Andrew Bunker [27], Elisa Cataldi [28,29,30], Stephane Charlot [20], Giovanni Cresci [30], Mirko Curti [28], Andrew C. Fabian [10], Harley Katz [31,32], Nimisha Kumari [33], Nicolas Laporte [34], Giovanni Mazzolari [4], Brant Robertson [35], Fengwu Sun [36], Bruno Rodriguez Del Pino [5], Giacomo Venturi [22]



The recent discovery of a large number of massive black holes within the first two billion years after the Big Bang, as well as their peculiar properties, have been largely unexpected based on the extrapolation of the properties of luminous quasars [1–5]. These findings have prompted the development of several theoretical models for the early formation and growth of black holes [6–11], which are, however, difficult to differentiate. We report the metallicity measurement around a gravitationally lensed massive black hole at redshift 7.04, hosted in a galaxy with very low dynamical mass. The weakness of the [OIII]5007 emission line relative to the narrow H$\beta$ emission indicates an extremely low chemical enrichment, less than $10^{-2}$ solar. We argue that such properties cannot be uncommon among accreting black holes around this early cosmic epoch. Explaining such a low chemical enrichment in a system that has developed a massive black hole is challenging for most theories. Models assuming heavy black hole seeds (such as Direct Collapse Black Holes) or super-Eddington accretion scenarios struggle to explain the observations, although they can potentially reproduce the observed properties in rare cases. Models invoking "primordial black holes" (i.e. putative black holes formed shortly after the Big Bang) [12] may potentially explain the low chemical enrichment associated with this black hole.

Abell2744-QSO1 (hereafter QSO1) is a triply imaged lensed Active Galactic Nucleus (AGN) at $z = 7.04$, initially identified through JWST-NIRCam imaging [13] and then spectroscopically confirmed with low resolution, multi-object JWST-NIRSpec prism spectroscopy [14], as well as high resolution ($R \sim 2700$) NIRSpec integral field spectroscopy (IFS) [15,16]. The detection of broad H$\alpha$ and broad H$\beta$, typical of the Broad Line Region (BLR) of AGN, the presence of H$\alpha$ and H$\beta$ absorption, indicative of extremely high densities ($n > 10^9\ cm^{-3}$) typical of the BLR [15–17], and the variability signatures [15,18], have unambiguously revealed that Abell2744-QSO1 is hosting an accreting massive black hole. Using standard virial relations [19], a black hole mass of about $1.5 \times 10^7\ M_\odot$ is inferred (see Methods for a discussion of the uncertainties). The high resolution NIRSpec-IFS observations have also enabled an estimation of the dynamical mass of the host galaxy in the range $10^{7.1} - 10^8\ M_\odot$, which sets a tight upper limit on the stellar mass in the host galaxy [15,16].

We further exploit the high resolution NIRSpec-IFS data by focusing on the narrow components of the emission lines and their spatially resolved properties, with focus on their line ratios. Fig.1a shows the spectra extracted from the central 0.2″, i.e. from within the central r<150 pc (see Methods and Fig.1d), and reveals extremely weak [OIII]5007 emission. Such weak emission was also noticed by [14] in the low resolution, prism spectrum, but they could not assess the intensity relative to the corresponding narrow component of H$\beta$, because the latter is blended with the broad component coming from the BLR. In the new high resolution spectrum it is possible to spectrally resolve and disentangle the broad component of H$\beta$ ($FWHM \sim 2600$ km/s) from the narrow component ($FWHM < 75$ km/s), as illustrated in Fig.1a. We adopt the same fitting as in Ref. [15] to disentangle the narrow and broad H$\beta$ components, and which also includes an absorption component that is seen more clearly in the H$\alpha$ profile [16]. The spectrum extracted from the central 0.2″, subtracted of the broad component and continuum, is shown in Fig.1b, further highlighting the prominence of the narrow component of H$\beta$ (hereafter H$\beta_N$) and the weakness of [OIII]5007. H$\beta$ has a residual weak blue wing after subtracting the broad component, which is spatially resolved and probably associated with an outflow (Methods), and whose flux is not included in H$\beta_N$.

The inferred ratio between [OIII]5007 and H$\beta_N$ is extremely low, less than unity ([OIII]5007/H$\beta_N \sim 0.6$). Such an extremely low [OIII]/H$\beta_N$ ratio is very rarely found among high-z galaxies [20,21] and, in these low mass systems, is explained in terms of extremely low metallicity [22,23]. In the Methods we discuss that, unlike the H$\beta$ broad (from the BLR), alternative scenarios (such as extremely high density of the ISM or low ionization) for explaining the low [OIII]/H$\beta$ are physically implausible.

H$\beta_N$ has some spatial extension. This is noticeable in Fig.1d, which shows the radial profile of H$\beta_N$, compared with the radial profile of the broad component and the continuum (Methods). The continuum traces the Point Spread Function (PSF, given that the continuum source is unresolved even in the NIRCam images). The figure illustrates that, while a large fraction H$\beta_N$ comes from a very

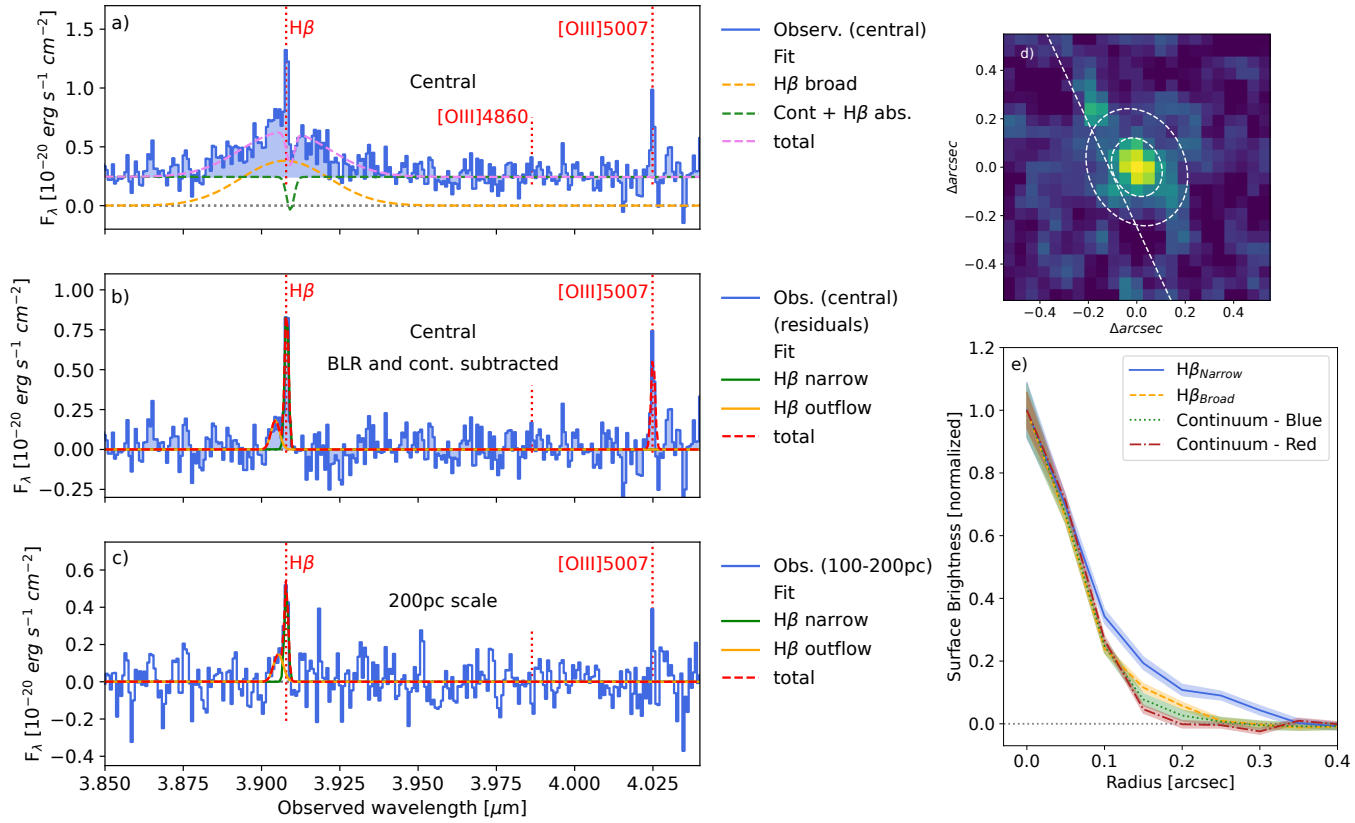


**Fig. 1 |** Left. Spectra of QSO1 around H$\beta$ and [OIII]5007. a) Spectrum extracted from the central region (blue solid line), with the fitted broad component of H$\beta$ (orange dashed line), continuum and H$\beta$ absorption (green dashed line), as in Ref. [15], while the violet dashed line shows the total fit. b) The same central spectrum where the broad H$\beta$, continuum and H$\beta$ absorption have been subtracted to highlight the narrow component of H$\beta$ and [OIII]5007. c) Spectrum extracted from a semi-annulus from 0.1″ (∼ 150 pc) to 0.2″ (∼ 300 pc) from the centre – H$\beta$ is clearly detected while [OIII]5007 is formally undetected (flux mostly on a single pixel). Right: d) Map of H$\beta$ narrow with overlayed the central aperture and annulus used for extracting the spectra in panels a,b and c, respectively; [OIII] falls in the detector gap in the region on the East (i.e. left) of the dashed straight line, hence this portion of the annulus was not used for extracting the spectrum. e) Radial profiles (normalized to the peak) of the narrow component of H$\beta$ (solid blue, the shaded area is 1$\sigma$ error on the mean), the broad component of H$\beta$ (dashed orange), the continuum on the blue side of H$\beta$ (dotted green) and the continuum on the red side of H$\beta$ (dot-dashed red), which trace the PSF; the narrow component has a compact core but it also shows a clear extended component.

compact, unresolved region, it also has a component extending on scales of ∼ 0.2″ (∼ 300 pc deprojected). The broad component of H$\beta$ has some indication of extension, likely because it includes the weak blue wing (with smaller width relative to the broad component) that is probably tracing an outflow.

In Fig.1c we also show the spectrum extracted from a semi-annulus between 0.1″ and 0.2″ (150-300 pc) from centre, where we had to exclude the South-West part of the annulus because of [OIII] falling in the detectors gap in that region (Methods). The broad H$\beta$ is undetected. There is a weak blue wing which may originate from a mild outflow, as discussed above. Yet, the most important finding is that H$\beta_N$ is still clearly detected. There is only a weak hint of [OIII]5007, which is formally undetected (the putative flux is only on one single spectral pixel, narrower than the line spread function). The inferred upper limit of the narrow line ratio in this annulus is even lower than in the central region: [OIII]/H$\beta_N$ < 0.32 (3$\sigma$).

As discussed in Ref. [16], given the extremely narrow width of [OIII], H$\beta_N$ and H$\alpha_N$, these components are likely powered by star formation in the host. We therefore infer the metallicity by using the calibrations recently derived for high-$z$ star forming galaxies. In the Methods we show that the results would hold also assuming photoionization by the AGN. Fig. 2a shows the location of QSO1 on the [OIII]/H$\beta$ versus metallicity diagram, calibrated by Ref. [24] (red solid line) on high-$z$ galaxies (small blue points, while green squares indicate additional high-z galaxies at low metallicity not included in the calibrations [25–27]). This calibration provides a metallicity $8 \times 10^{-3}$ $Z_\odot$ for the central region, and an upper limit of $6 \times 10^{-3}$ $Z_\odot$ for the extended region (based on the 3$\sigma$ upper limit on [OIII]/H$\beta$). There is potentially a highly super-solar solution (high metallicity branch) that, in addition to being highly implausible for such a small system at such high redshift, is ruled out (shaded region) by the weakness of the low ionization lines ([OII]3727 and [SII]6720, Methods).

Fig. 2b shows also the calibration using the parameter $\hat{R} = 0.46\ \log([OII]/H\beta) + 0.88\ \log([OIII]/H\beta)$, for which we only have upper limits, but which give an upper limit on the metallicity ($Z < 10^{-2}\ Z_\odot$) consistent with the values in Fig. 2a. Dashes and dot-dashed lines show other calibrations obtained at high-z [28,29], which would give even lower metallicities.

In most scenarios of black hole-galaxy co-evolution it is difficult to grow a black hole with masses in excess of $10^7\ M_\odot$ while keeping the metallicity of the interstellar medium as low as $10^{-2}\ Z_\odot$. Therefore, this finding is indicative of some specific route that allowed the black hole to form and grow in a very un-evolved stellar system.

Fig. 3 shows the location of QSO1 on the metallicity versus black hole mass plane, and versus black hole to stellar mass ratio. The golden symbol is for the central region (r<150 pc) while the orange

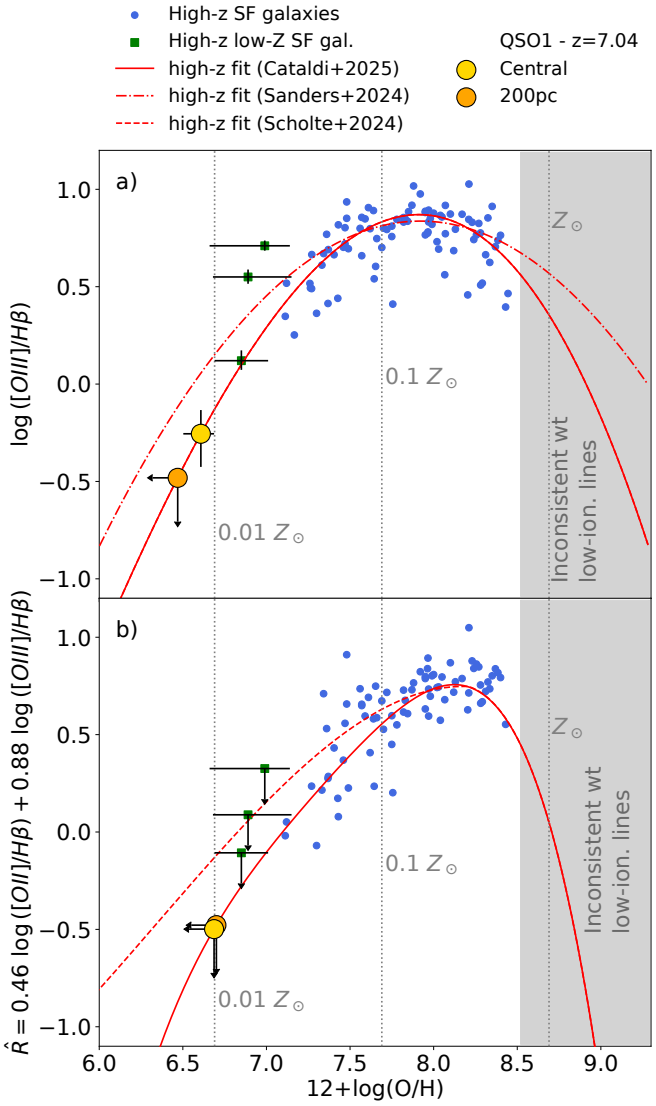


**Fig. 2 |** Metallicity constraints on QSO1 inferred from the observed emission line ratios. The red solid lines show the calibrations of [OIII]/H$\beta$ (a) and $\hat{R} = 0.46\,R_2 + 0.88\,R_3$ (b) from Ref. [24] using high-z star forming galaxies (small blue point). Green squares are other high-z galaxies at low metallicity [25–27] which were not included in the calibration. The QSO1 line ratios are shown with large circles, yellow and orange for the central region and for the outer region at ~200 pc, respectively. The dot-dashed and dashed lines show other calibrations at high-z [28,29], which would give even lower metallicities for QSO1. The shaded area indicate the high metallicity solutions excluded by the low ionization lines (Methods).

symbol is for the semi-annulus at r~200 pc from the centre. The $M_{BH}/M_{star}$ estimates for QSO1 are all lower limits as stellar light is not clearly detected [15,16], but an upper limit on the stellar mass can be inferred from the dynamical mass [15,16] (Methods). In Fig. 3a the contours show the distribution of semi-analytical models (SAMs) at $z$=7 which assume super-Eddington accretion. In all plots the outermost contour includes 99% of the distribution. Green solid contours are for models from the DELPHI SAMs models [84] with light seeds (100 $M_\odot$) that are allowed to accrete at up to 5 times higher than the Eddington limit. The dashed brown contours are from the SAM CAT models [31] involving both light and heavy seeds ($10^2 - 10^5$ $M_\odot$) allowed to accrete up to tens of times above Eddington for short phases. These SAM models struggle to reproduce the observations – less than 1% of them can barely match the observed properties of QSO1.

While in the Methods we discuss that is unlikely that the black hole mass is uncertain by more than a factor of a few, even assuming that this quantity is highly uncertain, the black hole mass is not the main issue when comparing our observations with these models - the main constraining property, and difficult to reproduce, is the very low metallicity.

Fig. 3b shows the DELPHI and CAT models at $z$=7 in the scenario of heavy seeds ($10^3 - 10^5$ $M_\odot$) whose accretion is Eddington limited. These scenarios can reach lower metallicity at $z$~7 relative to the super-Eddington model. The primary reason is that in the super-Eddington models the excess of gas inflow required to boost BH accretion also results in boosting star formation that rapidly enriches the ISM. Note that the CAT SAMs have a metallicity floor that is given by the modelling assumption that the IGM metallicity at this epoch is $\log(Z_{IGM}/Z_\odot) = -2.5$ (horizontal dashed line). Both these Eddington-limited models struggle to achieve the required black hole mass, or $M_{BH}/M_{star}$ ratio at the appropriate metallicity.

Fig. 3c illustrates the case of the AESOPICA hydrodynamical simulations based on the FABLE model [32] with modifications to the BH modelling [33] to allow for very high accretion rates up to 10 times the Eddington limit. Orange dashed contours show the case of heavy seeds ($10^5$ $M_\odot$), while gray solid contours show the case of the upper boundary for light seeds ($10^3$ $M_\odot$). In these hydrodynamical simulations light seeds, even accreting at super-Eddington rates, are completely excluded. The case of heavy seeds also struggles to reproduce QSO1 because of its low metallicity, but also because of the high $M_{BH}$ and high $M_{BH}/M_{star}$. There are very few cases where such low metallicity is reached at $z = 7$, in less than 1% of the simulations.

Fig. 3d shows the case of "primordial black holes" (PBHs), i.e. black holes that, according to some scenarios, might have formed in the ultra-early universe, in the first second after the Big Bang, possibly reaching back to the inflationary era [12]. Although the relevance of PBHs as dominant dark matter candidates has been mostly ruled out, they are still considered viable as seeds for the subsequent growth of massive black holes. In this scenario, black holes would be the very first structures formed in the Universe, much earlier than stars. The expected mass function of primordial BHs is very uncertain, partly because they are expected to be very clustered, possibly causing them to rapidly merge hierarchically. The blue contours in Fig. 3d show a version of the PHANES analytic model [9] in which the growth of halos and their baryonic components is seeded by primordial BHs (Methods). This model can reproduce QSO1 within 10% of the distribution, i.e. reasonably well considering the uncertainties associated with this class of black holes. The red tracks show the result of hydrodynamical simulations [34], which follow the evolution of primordial black holes (assuming the case of $10^6$ $M_\odot$ PBHs), in their final snapshots from $z$=10 to 9 (the properties are not expected to change significantly at $z = 7$). As illustrated, in these hydrodynamical simulations the assumed BH mass increases very little in this short epoch (but see Methods for limits on its growth), whereas the metallicity and $M_{star}$ evolve with time and depending on the object. Overall, these hydrodynamical simulations incorporating PBHs can also potentially explain the properties of QSO1, although subject to the specific assumptions underlying the metallicity evolution and the assumed initial mass of the PBH.

We note that QSO1-like BHs cannot be so uncommon. Indeed, QSO1 is one of the two BHs found at $z$>7 in the UNCOVER survey [35], and the only one with $M_{BH} < 10^8$ $M_\odot$. Additionally, it is found in a

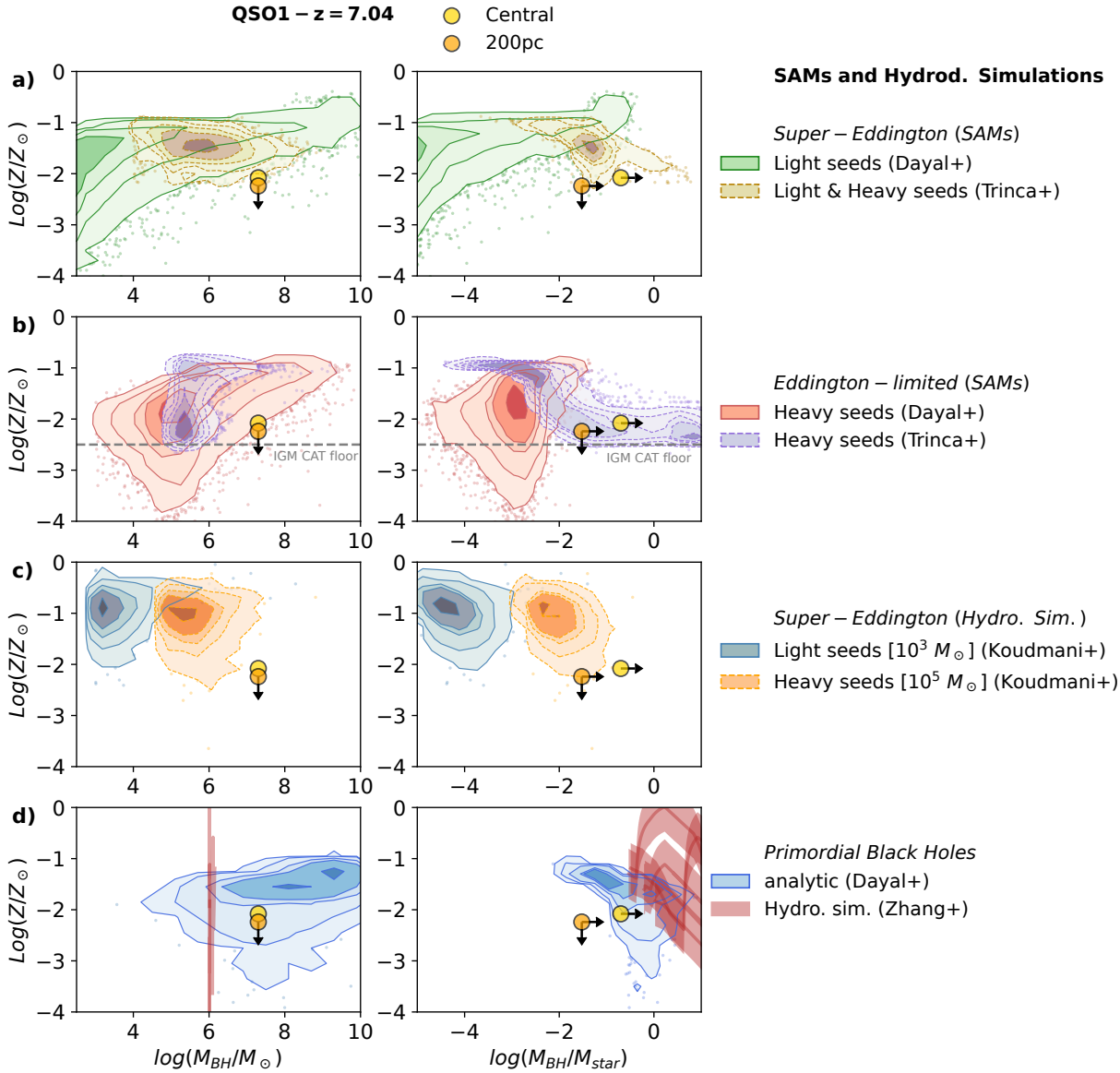


**Fig. 3 |** Comparison of the QSO1 properties with Semi-Analytical Models (SAMs) and Hydrodynamical Simulations on the metallicity versus $M_{BH}$ and metallicity versus $M_{BH}/M_{star}$ diagrams. Description of all models are provided in the text and in the Methods. Contours enclose 1%, 30%, 68%, 84%, 95%, and 99% of the models or simulations. Models/simulations outside the 99% countours are plotted individually. For the PBH hydrodynamical simulations red lines show the evolution of four select cases and the shaded regions indicate the uncertainty on the metallicity. The golden and orange circle show the properties of QSO1 in the central aperture and in the outer annulus (~ 200 pc from the centre), respectively.

very small sky area close to the caustic behind the Abell 2744 field (within ~30″) that could produce multiple images, meaning that the volume density of these type of objects cannot be low. Finally, there might be other similar cases at z>7, as discussed below. Therefore, it is very unlikely that QSO1 is an outlier, and implausible that it is in the tail of a distribution with probability to be found of less than a few percent – QSO1-like systems must be fairly common among intermediate mass BHs ($M_{BH}$ a few times $10^7$ $M_\odot$) at $z$>7.

As a consequence, the fact that heavy seeds or super-Eddington models and simulations reproduce the properties of QSO1 only in less than 1% of the cases, highlights some potential problems in these scenarios. It may indicate that these models require additional, major pristine gas inflows to dilute the metallicity. Additionally, stronger feedback processes may be at work, both ejecting metals more efficiently and/or suppressing star formation (and hence the production of metals) more effectively. Alternatively, the underlying BH seeding and growth assumptions may not be adequate to reproduce this population of objects in the early Universe. On the other hand, the fact that scenarios invoking PBHs can explain the properties of QSO1-like system, including their seemingly high space density, indicates that the physics behind this model may actually account for a significant population of early BHs. Finally, we caution that all these comparisons with models are done assuming that, at a given BH mass, the accretion rate is not dependent on metallicity. Yet, AGN duty cycles certainly play a role in their detectability, which should be taken into account in future studies.

As mentioned, it is important to compare QSO1 with other AGN1 at z>7. Aside from QSO1, there are six type 1 AGN found at $z$>7[35–41]. One of them has an estimated very low metallicity of $Z < 0.1\ Z_\odot$[38] and two more have very weak [OIII]5007 (although

its [OIII]/H$\beta_N$ is difficult to constrain due to low spectral resolution)[40,41], so these might share similar properties as QSO1. However the other three AGN have [OIII]/H$\beta$ significantly higher than in QSO1 and likely higher metallicity. Therefore, the origin of these other BHs may well be different from the one in QSO1. Most of them also have masses much higher than QSO1 and may have formed and grown through different channels.

## References


1. Matthee J., et al., 2023. Little Red Dots: an abundant population of faint AGN at $z \sim 5$ revealed by the EIGER and FRESCO JWST surveys, p. arXiv:2306.05448 arXiv:2306.05448
2. Kocevski D. D., et al., 2023. Hidden Little Monsters: Spectroscopic Identification of Low-mass, Broad-line AGNs at z > 5 with CEERS, ApJ, 954, L4
3. Maiolino R., et al., 2024. JADES: The diverse population of infant black holes at 4 < z < 11: Merging, tiny, poor, but mighty, A&A, 691, A145
4. Taylor A. J., et al., 2024. Broad-Line AGN at $3.5 < z < 6$: The Black Hole Mass Function and a Connection with Little Red Dots, p. arXiv:2409.06772 arXiv:2409.06772
5. Juodžbalis I., et al., 2025. JADES: comprehensive census of broad-line AGN from Reionization to Cosmic Noon revealed by JWST, p. arXiv:2504.03551 arXiv:2504.03551
6. Schneider R., et al., 2023. Are we surprised to find SMBHs with JWST at z ≥ 9?, MNRAS, 526, 3250
7. Natarajan P., et al., 2024. First Detection of an Overmassive Black Hole Galaxy UHZ1: Evidence for Heavy Black Hole Seed Formation from Direct Collapse, ApJ, 960, L1
8. Volonteri M., Habouzit M., Colpi M., 2023. What if young z > 9 JWST galaxies hosted massive black holes?, MNRAS, 521, 241
9. Dayal P., 2024. Exploring a primordial solution for early black holes detected with JWST, A&A, 690, A182
10. Dekel A., et al., 2025. Growth of massive black holes in FFB galaxies at cosmic dawn, A&A, 695, A97
11. Jeon J., Bromm V., Liu B., Finkelstein S. L., 2025. Physical Pathways for JWST-observed Supermassive Black Holes in the Early Universe, ApJ, 979, 127
12. Escrivà A., Kühnel F., Tada Y., 2024. in Arca Sedda M., Bortolas E., Spera M., eds, . Black Holes in the Era of Gravitational-Wave Astronomy. pp 261–377, doi:10.1016/B978-0-32-395636-9.00012-8
13. Furtak L. J., et al., 2023. JWST UNCOVER: Extremely Red and Compact Object at z = 7.6 Triply Imaged by A2744, ApJ, 952, 142
14. Furtak L. J., et al., 2024. A high black-hole-to-host mass ratio in a lensed AGN in the early Universe, Nature, 628, 57
15. Ji X., et al., 2025. BlackTHUNDER – A non-stellar Balmer break in a black hole-dominated little red dot at $z = 7.04$, p. arXiv:2501.13082 arXiv:2501.13082
16. D'Eugenio F., et al., 2025. BlackTHUNDER strikes twice: rest-frame Balmer-line absorption and high Eddington accretion rate in a Little Red Dot at $z = 7.04$, p. arXiv:2503.11752 arXiv:2503.11752
17. Juodžbalis I., et al., 2024. JADES - the Rosetta stone of JWST-discovered AGN: deciphering the intriguing nature of early AGN, MNRAS, 535, 853
18. Furtak L. J., et al., 2025. Investigating photometric and spectroscopic variability in the multiply-imaged Little Red Dot A2744-QSO1, p. arXiv:2502.07875 arXiv:2502.07875
19. Reines A. E., Volonteri M., 2016. in American Astronomical Society Meeting Abstracts #227. p. 119.01
20. Vanzella E., et al., 2023. An extremely metal-poor star complex in the reionization era: Approaching Population III stars with JWST, A&A, 678, A173
21. Curti M., et al., 2023. JADES: Insights on the low-mass end of the mass–metallicity–star-formation rate relation at $3 < z < 10$ from deep JWST/NIRSpec spectroscopy, p. arXiv:2304.08516 arXiv:2304.08516
22. Nakajima K., et al., 2022. EMPRESS. V. Metallicity Diagnostics of Galaxies over 12 + log(O/H) = 6.9-8.9 Established by a Local Galaxy Census: Preparing for JWST Spectroscopy, ApJS, 262, 3
23. Nakajima K., Maiolino R., 2022. Diagnostics for PopIII galaxies and direct collapse black holes in the early universe, MNRAS, 513, 5134
24. Cataldi E., et al., 2025. MARTA: Temperature-temperature relationships and strong-line metallicity calibrations from multiple auroral lines detections at cosmic noon, p. arXiv:2504.03839 arXiv:2504.03839
25. Willott C. J., et al., 2025. In Search of the First Stars: An Ultra-Compact and Very Low Metallicity Lyman-$\alpha$ Emitter Deep Within the Epoch of Reionization, p. arXiv:2502.07733 arXiv:2502.07733
26. Cullen F., et al., 2025. The JWST EXCELS survey: an extremely metal-poor galaxy at z = 8.271 hosting an unusual population of massive stars, MNRAS,
27. Mowla L., et al., 2024. Formation of a low-mass galaxy from star clusters in a 600-million-year-old Universe, Nature, 636, 332
28. Sanders R. L., Shapley A. E., Topping M. W., Reddy N. A., Brammer G. B., 2024. Direct T $_e$-based Metallicities of z = 2–9 Galaxies with JWST/NIRSpec: Empirical Metallicity Calibrations Applicable from Reionization to Cosmic Noon, ApJ, 962, 24
29. Scholte D., et al., 2025. The JWST EXCELS survey: Probing strong-line diagnostics and the chemical evolution of galaxies over cosmic time using $T_e$-metallicities, MNRAS,
84. Dayal P., et al., 2025. UNCOVERing the contribution of black holes to reionization, A&A, 697, A211
31. Trinca A., et al., 2024. Episodic super-Eddington accretion as a clue to Overmassive Black Holes in the early Universe, p. arXiv:2412.14248 arXiv:2412.14248
32. Henden N. A., Puchwein E., Shen S., Sijacki D., 2018. The FABLE simulations: a feedback model for galaxies, groups, and clusters, MNRAS, 479, 5385
33. Koudmani S., Sijacki D., Smith M. C., 2022. Two can play at that game: constraining the role of supernova and AGN feedback in dwarf galaxies with cosmological zoom-in simulations, MNRAS, 516, 2112
34. Zhang S., et al., 2025. How do Massive Primordial Black Holes Impact the Formation of the First Stars and Galaxies?, p. arXiv:2503.17585 arXiv:2503.17585
35. Greene J. E., et al., 2024. UNCOVER Spectroscopy Confirms the Surprising Ubiquity of Active Galactic Nuclei in Red Sources at z > 5, ApJ, 964, 39
36. Kokorev V., et al., 2023. UNCOVER: A NIRSpec Identification of a Broad-line AGN at z = 8.50, ApJ, 957, L7
37. Maiolino R., et al., 2024. A small and vigorous black hole in the early Universe, Nature, 627, 59
38. Tripodi R., et al., 2024. Red, hot, and very metal poor: extreme properties of a massive accreting black hole in the first 500 Myr, p. arXiv:2412.04983 arXiv:2412.04983
39. Übler H., et al., 2024. GA-NIFS: JWST discovers an offset AGN 740 million years after the big bang, MNRAS, 531, 355

40. Taylor A. J., et al., 2025. CAPERS-LRD-z9: A Gas Enshrouded Little Red Dot Hosting a Broad-line AGN at z=9.288, p. arXiv:2505.04609 arXiv:2505.04609
41. Naidu R. P., et al., 2025. A “Black Hole Star” Reveals the Remarkable Gas-Enshrouded Hearts of the Little Red Dots, p. arXiv:2503.16596 arXiv:2503.16596
65. Übler H., et al., 2023. GA-NIFS: A massive black hole in a low-metallicity AGN at z ∼ 5.55 revealed by JWST/NIRSpec IFS, A&A, 677, A145
43. Harikane Y., et al., 2023. A JWST/NIRSpec First Census of Broad-Line AGNs at z=4-7: Detection of 10 Faint AGNs with M_BH∼10$\hat{6}$-10$\hat{8}$ M_sun and Their Host Galaxy Properties, p. arXiv:2303.11946 arXiv:2303.11946
44. Maiolino R., et al., 2024. JWST meets Chandra: a large population of Compton thick, feedback-free, and X-ray weak AGN, with a sprinkle of SNe, p. arXiv:2405.00504 arXiv:2405.00504
45. Costa G., et al., 2025. Evolutionary tracks, ejecta, and ionizing photons from intermediate-mass to very massive stars with PARSEC, Astron. Astrophys., 694, A193

# Methods

### Cosmology and conventions

A flat ΛCDM cosmology is adopted throughout based on the latest results of the Planck collaboration [46], with $H_0 = 67.4\,\mathrm{km\,s^{-1}\,Mpc^{-1}}$, $\Omega_\mathrm{m} = 0.315$, $\Omega_\mathrm{b} = 0.0492$. At $z = 7.04$, an on-sky separation of 1″ corresponds to 5.53 physical kpc (pkpc). The lensing magnification results into a stretching of this scale by a factor of about 3.5 [14].

### Spectral extraction and data analysis

We used the NIRSpec-IFS spectral cubes from the BlackTHUNDER programme PID-5015 already presented in Ref. [15] and Ref. [16]. The observations and data processing are extensively discussed in the latter two papers. Here we simply recall that the observations targeted image A of QSO1 (lensing magnification factor $\mu \sim 5.8 - 6.15$, depending on the adopted model [14,15]) with the NIRSpec IFU mode, both with the high resolution disperser G395H (for a total exposure of 7.4 hours) and with the low resolution prism (for a total of 2 hours), although the latter is not used in this paper.

The Point Spread Function (PSF) of the IFU observations is difficult to determine, as it does not follow exactly the JWST theoretical PSF – it also tends to be slightly elongated along the direction of the IFU's slices [47]. In the case of QSO1 we leverage the fact that the continuum is unresolved, based on the NIRCam images [14] and therefore we can take the continuum as a reference to trace the PSF. We find that the continuum between H$\beta$ and [OIII] (the spectral region of main interest), is well described by an ellipse with axial ratio 0.8 and major axis $PA = -25°$.

To avoid degeneracies in the decomposition between the broad and narrow emission components, we conservatively created the map of $H\beta_N$ shown in Fig.1d by simply collapsing the three spectral channels around the peak of $H\beta_N$. This implies that the map includes also some contribution from the broad line, but this does not affect our result as the map is not used for quantitative purposes. Similarly, for simplicity and to avoid degeneracies, the radial profile of H$\beta_N$ shown in Fig.1e (blue solid line) is obtained by simply collapsing the three spectral channels around the peak of $H\beta_N$; this is conservative as it implies that the actual radial profile of $H\beta_N$ is probably even more extended. As mentioned, given that the continuum is not resolved in the NIRCam images, it can be used to trace the PSF. We have extracted the profile of the continuum blueward of $H\beta$ by collapsing the spectral channels in the region 3.700–3.835 $\mu$m (green dashed line), and the profile of the continuum redward of H$\beta$ by collapsing the spectral channels in the region 3.944–3.700 $\mu$m (red dot-dashed line). The profile of broad $H\beta$ (dashed orange line) is extracted from the high S/N region between 3.894–3.904 $\mu$m; this also includes part of the "blue wing", which we tentatively ascribe to a low metallicity outflow, on the grounds that this profile is slightly more extended than the continuum and also seen in the outer annulus, as dicussed below.

We extract the central spectrum around H$\beta$ with an elliptical aperture with the same shape and orientation as the PSF and with minor axis of 0.2″ and major axis 0.5″ (Fig.1d); this is nearly identical to the aperture adopted by [15] and [16]. The outer spectrum is extracted from an annulus with the same shape and covering the region between the central aperture and an outer ellipse with minor axis of 0.4″ (Fig.1e). However, unfortunately, the [OIII] enters the the detector gap (for some dithers) in the region to the East of the dashed line indicated in Fig.1d, which makes the [OIII] flux unreliable in that area, so we have excluded that region from the spectral extraction.

| | | |
|---|---|---|
| $F([OIII]5007)/F(H\beta_N)$ | (central) | $0.55 \pm 0.18$ |
| $F([OIII]5007)/F(H\beta_N))$ | (R∼200) | $< 0.33$ |
| $F([OIII]5007)/F([OII]3727)$ | (central) | $> 3.1$ |
| $F([OIII]4363)/F([OIII]5007)$ | (central) | $< 0.30$ |
| $F([NII]6584)/F(H\alpha_N)$ | (central) | $< 0.29$ |
| $F([SII]6717,6731)/F(H\alpha_N)$ | (central) | $< 0.08$ |

**Extended Data Table 1 |** Flux ratios for the narrow emission lines.

The lines were fitted with Gaussians, with the requirement that their width cannot be smaller than the NIRSpec spectral resolution at that wavelength [48,49]. In addition to the narrow component, fitting of H$\beta$ involved two broad components and an absorption component, which are shown in Fig.1a-b. We do not expand on this, as the methodology is very similar to that adopted by [15] and [16], which both find the same [OIII]/H$\beta \sim 0.6$ ratio for the central region, independent of the method adopted to fit the broad component. However, we note that narrow broad component is extended, as inferred from the outer spectrum in Fig.1c, and therefore it may be tracing a low metallicity outflow; this has implications for the estimation of the black hole mass, which will be discussed further below.

Ref. [15] and Ref. [16] extract spectra from a central aperture, very similar to ours. The apertures are approximatively matched to the PSF at each wavelength (hence different apertures around H$\beta$ and H$\alpha$) so to maximize the S/N, and then aperture corrections are applied. Yet, this is appropriate for the unresolved components (broad lines and continuum); however, our finding that the narrow component of H$\beta$ is extended implies that the aperture correction is more complex. As a consequence, here we do not aim at providing the absolute fluxes of the narrow emission lines, but only the line ratios in pairs that are relatively close in wavelength (hence whose aperture corrections are very similar), and which are relevant for this paper. The inferred narrow line ratios are reported in Extended Data Table1.

Extended Data Fig.1 shows portions of the spectrum extracted from the central region around the expected wavelengths of the [OII]3726,3729, [OIII]4363 and [SII]6716,6731 doublet, to illustrate the non detections. [OIII]4363 shows a hint of emission, but significantly offset from the expected wavelength, so we do not consider it a detection, while it might be associated with the broad component of H$\gamma$.

### Dust extinction

Previous works have inferred some amount of dust extinction in QSO1. In particular, Ref. [16] derive an extinction $A_V = 1.4$ based on the narrow components of the H$\alpha$ and H$\beta$, and assuming an Small Magellanic Cloud (SMC)-like extinction curve. However, in order to optimize the S/N, they extracted H$\alpha$ from an aperture larger than H$\beta$, so to take into account the larger PSF (and then applying aperture corrections). This procedure is appropriate for the broad lines, as they are spatially unresolved. However, we have now found that the narrow components are extended. As a consequence, the larger aperture used for H$\alpha$ has also incorporated more extended flux. Based on the (higher resolution) H$\beta_N$ profile, we estimate that the H$\alpha_N$ flux given in Ref. [16] should be corrected by a factor of 0.73 in order to be properly compared with $H\beta_N$. Once this correction is applied, the inferred dust extinction drops to $A_V = 0.66 \pm 0.40$.

It is worth mentioning that a very low metallicity is also independently derived by Ref. [16] who infer a very low dust content, specifically $Z\xi_d < 8\times10^{-4}$, where $\xi_d$ is the dust-to-metal ratio. Assuming an evolution of $\xi_d$ as a function of $Z$ as obtained by Ref. [50], this would imply $Z < 10^{-2}\ Z_\odot$. The lower value of $A_V$ obtained by us reduces

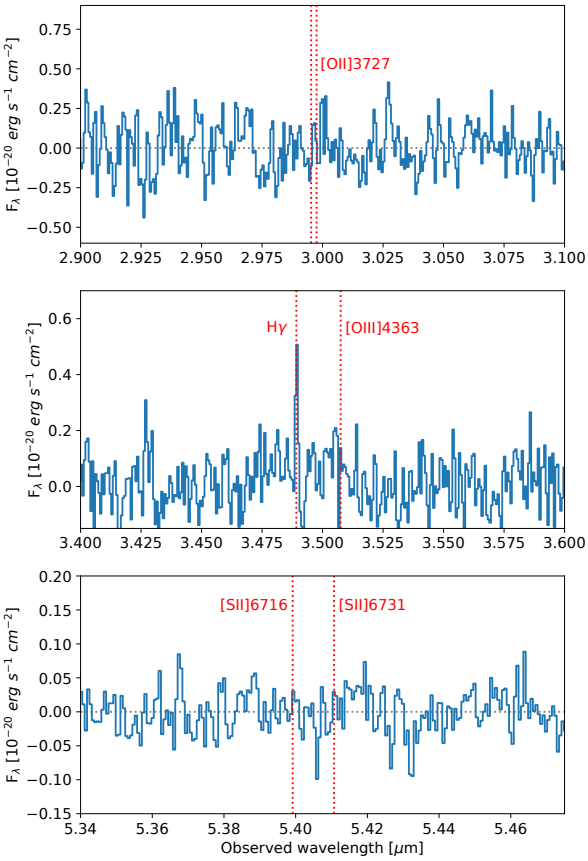


**Extended Data Fig. 1 |** Portion of spectra extracted from the central aperture illustrating the non detections of [OII]3727, [OIII]4363 and [SII]6716,6731.

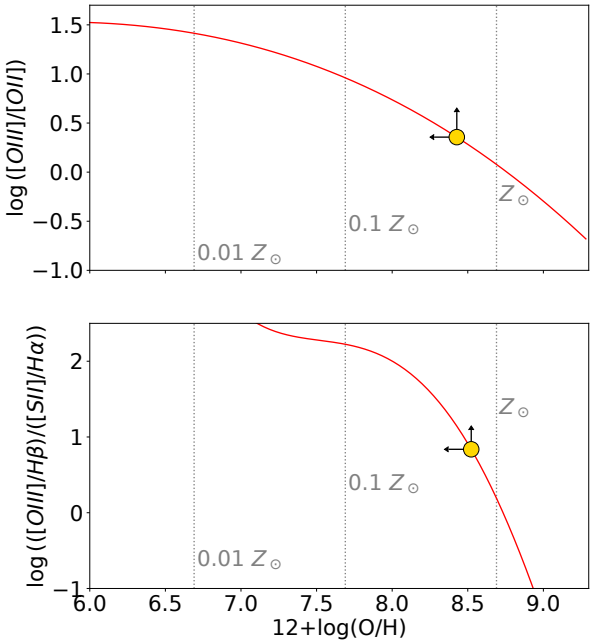


**Extended Data Fig. 2 |** Constraints on the metallicity from the non-detection of low ionization lines. Top: log([OIII]5007/[OII]3727) lines flux ratio versus metallicity according to the calibration obtained by Ref.[24] at high-z (red line). Bottom: log(([OIII]5007/H$\beta$)/([SII]6716,6731/H$\alpha$)) as a function of metallicity according to the local relation identified by Ref.[55]. In both panels the golden symbols indicate the 3$\sigma$ limits obtained for QSO1, both of which exclude the highly super-solar metallicity solution of the [OIII]/H$\beta$ value.

even further the estimated upper limit on the product of metallicity and dust-to-metal ratio, specifically $Z\xi_d < 4 \times 10^{-4}$, hence reduces even further the inferred metallicity with this method.

We finally further clarify that the presence of some dust extinction is not incompatible with the extremely low metallicity inferred in this paper. To begin with, the new value of extinction is consistent with zero within 1.5$\sigma$. Secondly, we can estimate the expected dust absorption in this system given the metallicity and size. Assuming, to a first order, a constant dust-to-metal ratio, we can approximatively infer the expected extinction as

$$A_V = \left(\frac{A_V}{N_H}\right)_{MW} \xi_{d.MW} \frac{Z}{Z_{MW}} N_H$$

where $\left(\frac{A_V}{N_H}\right)_{MW} = 4.7 \times 10^{-23}\ mag\ cm^2$ is the extinction-to-gas column density ratio measured for the Milky Way[51]; $\xi_{d.MW} = 0.45$ is the average dust-to-metal ratio in the MW[50]; $Z_{MW} = 0.6\ Z_\odot$ is the average metallicity at the MW locations where the $\xi_{d.MW}$ measurements were performed. The column of gas can be approximatively given by $N_H \approx R\ n$, where $R$ is the size of the gaseous system and $n$ the average gas density. Given that H$\beta_N$ extends up to ~0.25″, i.e. ~ 400 $pc$, the previous equation gives

$$A_V \approx 3.6\ 10^{-4}\ \frac{n}{cm^{-3}}\ mag$$

Therefore, to obtain an extinction of $A_V = 0.66 \pm 0.40$ mag it would only take a gas density of ~ $(2 \pm 1.2) \times 10^3$ cm$^{-3}$, which is well within the value typically estimated from the optical lines for such high-z galaxies ($10^2 - 10^4$ cm$^{-3}$)[76,77]. Yet, assuming uniform density is certainly an oversimplification. A more realistic density distribution is that of an exponentially declining density, $n \propto R^-\alpha$, typically with $\alpha = 2$. In the latter case the equation above becames

$$A_V \approx 1.4 \times 10^{-2}\ \frac{n_{r400}}{cm^{-3}}\ \text{mag}$$

where $n_{r400}$ is the gas density at a radius of 400 pc. From the latter equation, an extinction $A_V = 0.66 \pm 0.40$ mag would imply a gas density $n_{r400} \approx 50$ cm$^{-3}$, which would be consistent with the values inferred from the far-IR lines at high-z ($n < 500$ cm$^{-3}$)[52], which are indeed seen to be extended on a few 100 pc scales in these high-z systems[53,54].

### Ruling out the high metallicity solution

As discussed in the main text, for a given [OIII]/H$\beta$ ratio the metallicity calibration provided by Ref.[24] (as well as any other metallicity calibrations for [OIII]/H$\beta$) has two solutions, as illustrated in Fig.2. Therefore, in principle, the [OIII]/H$\beta$ value observed in QSO1 could also correspond to extremely high metallicity, more than two times solar. Such an extremely high metallicity would be totally implausible for such a low mass system at such high redshift (e.g.[21]) . Additionally, the high metallicity solution can be ruled out based on the upper limits on the low ionization lines. Indeed, the ratio [OIII]/[OII] has a monotonic dependence on metallicity, which has also been calibrated for high-z galaxies[24], as shown in Extended Data Fig.2-top. The lower limit on the [OIII]/[OII] ratio in QSO1 implies a metallicity < 0.55 $Z_\odot$, hence completely ruling out the supersolar solution of [OIII]/H$\beta$. The upper limit on [SII]/H$\alpha$ is also informative. Indeed, Ref.[55] showed that the ratio $O3S2 = \frac{[OIII]/H\beta}{[SII]/H\alpha}$ is monotonically decreasing with metallicity. Unfortunately, this diagnostic has not been calibrated at high-z. However, using the local relation, shown

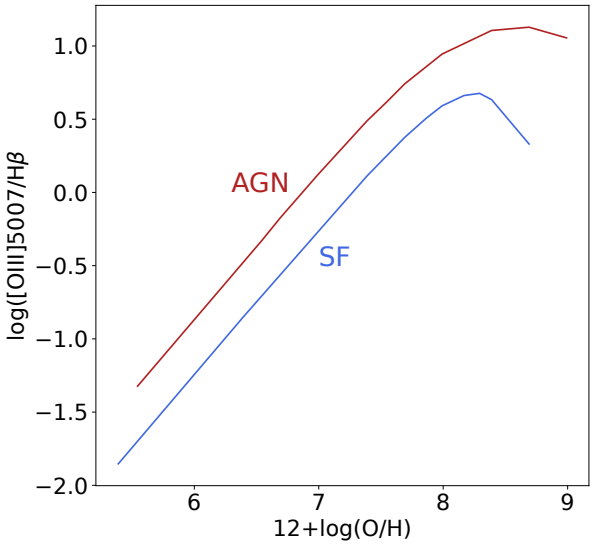


**Extended Data Fig. 3 |** [OIII]5007/H$\beta$ flux ratio as a function of metallicity for AGN (red) and Star Formation (blue) models, as discussed in the text. In the low metallicity (sub-solar) branch, a given [OIII]/H$\beta$ ratio resulting AGN photoionization would result into an even lower metallicity than the star formation case.

in Extended Data Fig.2-bottom, and the 3$\sigma$ lower limits obtained for QSO1 reported in Tab.1, we obtain a lower limit on the metallicity of $< 0.67\ Z_{\odot}$, once again excluding the highly supersolar metallicity solution of [OIII]/H$\beta$.

### AGN excitation of narrow lines

In the main text we have assumed, following Ref.[16], that the narrow emission lines are excited by star formation. Ref.[16] motivated this by the extremely narrow width of the lines. Here we discuss the scenario in which the narrow lines are excited by the AGN, i.e. are part of a Narrow Line Region, although in this case one would expect broader lines because of feedback from AGN radiation pressure.

The calibration obtained by Ref.[24] for high-z star forming galaxies is not expected to change significantly in the case of AGN. Indeed, high-z galaxies are characterized by very high ionization parameters, similar to the AGN, and tend to have harder ionizing spectrum, akin AGN, because of their reduced iron content[60,61]. At the same time, high-z AGN are characterized by softer ionizing spectra than local AGN, akin star forming galaxies, as indicated by the weakness of high-ionization lines[62]. Therefore, the physical conditions and ionization of high-z star forming galaxies and the NLR of high-z AGN are expected to be similar. Indeed, it is known that in many traditional narrow line diagnostic diagrams high-z AGN and high-z SF galaxies largely overlap[65,3,5]; this makes the identification of narrow line (type 2) AGN extremely difficult at high-z[63,64] and indeed the high-z sample used by Ref.[24] (and compilation in there), for the calibrations, may include a few high-z AGN according to some diagnostics. Therefore, the low metallicity inferred from the Ref.[24] calibration may likely hold also in the case of AGN photoionization of the narrow lines.

In any case, the harder ionization spectrum from an AGN, would make the [OIII]/H$\beta$ ratio even higher at a given metallicity, relative to star forming galaxies. We illustrate this in Extended Data Fig.3, where we show the example of the expected [OIII]/H$\beta$ ratio in the case of an AGN ionizing spectrum (red) and a star formation ionizing spectrum (blue), for a given ionization parameter $log\ U = -2$. We use the models presented in Ref.[23], where for the AGN we take the case of an ionizing spectrum modelled with a black body with temperature $2 \times 10^5\ K$ and power law $\alpha = -2$, while the BPASS models with age 1Myr age used for star forming galaxies. Clearly, in the low-metallicity branch, in case of AGN photoionization a given [OIII]/H$\beta$ ratio would give an even lower metallicity than inferred by assuming photoionization by star formation.

We, however, attempt to estimate the gas metallicity also independently of the Ref.[24] calibration. Extended Data Fig.4 shows the BPT-[NII] and BPT-[SII] diagnostic diagrams, which are typically used in the local Universe to differentiate star forming galaxies and AGN[56,57]. At high-z AGN mostly are distributed in the Star Forming region of the diagram[3,5,43,65]. The general interpretation is that the offset of high-z AGN on these diagnostic diagrams is that either the AGN ionizing radiation is filtered and does not reach the ISM to produce a NLR (hence the nebular narrow lines are dominated by star formation in the host galaxy)[44], or that it is a consequence of low gas metallicity in the host galaxy[65,3,43]. The latter scenario is illustrated by the AGN photoionization models plotted on the same diagrams (small starred symbols)[23], color-coded by metallicity, and clearly indicating a shift towards lower [OIII]/H$\beta$, lower [NII]/H$\alpha$ and lower [SII]/H$\alpha$ as the metallicity decreases. Interestingly, none of the high-z JWST-identified AGN in the JADES sample of Ref.[5] (with deep exposures) is detected in either [NII] or [SII]. A detection of [NII] and [SII] is obtained in the stack of the AGN at $3.5 < z < 5$, while these lines are not detected in the higher redshift stack at $5 < z < 7$. The values resulting from these high-z stacks are shown with a blue triangle and a red square in Extended Data Fig.4, respectively. The golden circle shows the upper limit for the spectrum extracted in the central region of QSO1 (where we have the highest S/N). The observed [NII]/H$\alpha$ upper limit is not very constraining, but the [SII]/H$\alpha$ upper limit is clearly far away from the local sequence and pointing at very low metallicities. Yet, it is reasonable to assume for QSO1 the same upper limit on the [NII]/H$\alpha$ and [SII]/H$\alpha$ ratios inferred from the JADES stack at $5 < z < 7$, as these are AGN at lower redshift and more massive than QSO1, and it is know that [NII]/H$\alpha$ and [SII]/H$\alpha$ increases towards lower redshift and higher masses. The gold and orange squares in Extended Data Fig.4 show the location of QSO1, for the central and outer spectrum respectively, assuming that QSO1 shares the same upper limits on [NII]/H$\alpha$ and [SII]/H$\alpha$ as the JADES stack at $5 < z < 7$. When compared with models, these reasonable, probably conservative, upper limits would indicate that QSO1 has a metallicity lower than $10^{-2}\ Z_{\odot}$.

### Black hole mass

Although the measurement of the black hole mass has a less critical role than metallicity, here we discuss how this has been estimated. The black hole in QSO1 has been estimated by Ref.[15] using the broad component of H$\beta$ and assuming the local virial relations[19,66], calibrated on reverberation mapping and direct BH mass measurements. These relations allow the black hole mass to be inferred based on the broad Balmer emission lines' luminosity and their width or dispersion. There have been discussions about the possibility that high-z AGN may not follow the local virial relations because they may be accreting at super-Eddington rates. It is not clear in what direction the correction should go – according to some models the BH masses might be overestimated by up to a factor of 5 for accretion rates 100 times higher than Eddington[62,67], while other models claim that the BH masses are *underestimated* even by orders of magnitude when accreting at Eddington or super Eddington rates[68,69]. However, it is

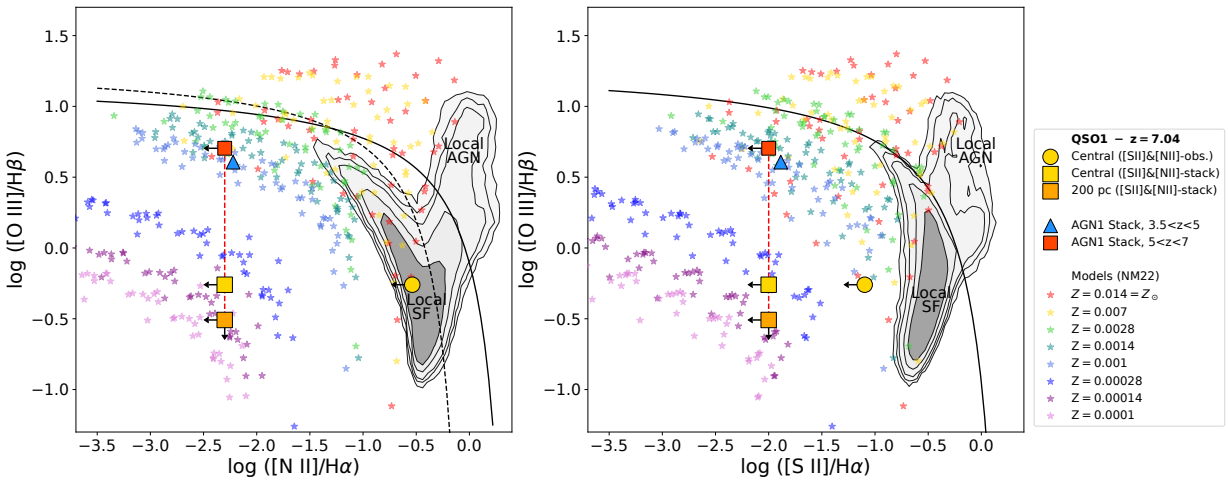


**Extended Data Fig. 4 |** BPT-VO98 diagnostic diagrams[56,57]. Left: log([OIII]5007/H$\beta$) vs log([NII]6584/H$\alpha$). Right: log([OIII]5007/H$\beta$) vs log([SII]6716,6731/H$\alpha$). In both diagrams contours show the distribution of local galaxies. The solid black line indicates the limit for maximal starburst identified by Ref.[58], while the black dashed line is the local demarcation between star forming galaxies and AGN identified by Ref.[59]. The blue triangle is the stack of AGN at $3.5 < z < 5$ while the red square is the stack of AGN at $5 < z < 7$ in the JWST selected sample of Ref.[5]. Small starred symbols are AGN photoionization models from Ref.[23] spanning different densities and ionization parameters, and color-coded by metallicity. The solid golden circle is the observation of QSO1 (central region), for which only relatively loose upper limits are available on [NII]/H$\alpha$ and [SII]/H$\alpha$, although the latter already excludes most high metallicity models. The golden and orange squares are the upper limits on the central and extended emission line ratios, respectively, where we have assumed that they have the same upper limit on [NII]/H$\alpha$ and [SII]/H$\alpha$ as the highest redshift AGN stack (although the galaxies in the stack are actually at redshift lower than QSO1 and are generally more massive). With this assumption the low [OIII]/H$\beta$ observed in QSO1 would clearly indicate a metallicity below $10^{-2}$ $Z_\odot$, consistent with the Star Forming calibration.

comforting that the direct black hole mass measurement via interferometry for a highly super-Eddington (7 – 20× Eddington) accreting case at $z = 2.6$ (i.e. at a cosmic epoch fairly close to the AGN investigated by JWST) gives a black hole mass that is within a factor 2.5 of the mass inferred by applying the virial relation to the H$\alpha$ broad component[70].

It has recently been claimed that the exponential-like profile of the H$\alpha$ broad component of some high-z AGN is due to electron scattering of a much narrower broad line, by an ionized medium with large column density embedding the central region[71]. This scenario would imply black hole masses much smaller than inferred by applying the virial relations. However, Ref.[5] have pointed out that such a scenario is not physically viable, as the ionized gas responsible for the scattering would produce a narrow emission H$\alpha$ an order of magnitude stronger than observed in high-z AGN. Additionally, exponential profiles of the broad lines are observed also in local AGN for which the black hole masses are estimated directly and are consistent with the virial relations[72,73].

Summarizing, there is not compelling evidence that black hole masses of high-z AGN are largely offset from what is estimated using the virial relations.

For what concerns QSO1, Ref.[15] derive a BH mass of $\log(M_{BH}/M_\odot) = 7.59$ based on the broad component of H$\beta$, with a single Gaussian fitting, and assuming an extinction of $A_V = 2.6$ based on the modelling of the continuum. However, the latter may be degenerate with the intrinsic continuum shape and other continuum components, and may be overestimated. Ref.[16] use the higher S/N and higher resolution observation of H$\alpha$ to infer a BH mass in the range $\log(M_{BH}/M_\odot) = 6.3 - 6.7$ (depending on the adopted virial calibration), assuming an extinction of $A_V = 1.4$ inferred from the narrow lines. However, we have discussed above that the narrow line extinction was likely overestimated and, when taking into account the different apertures and extension of the narrow components, the extinction is reduced to $A_V = 0.66 \pm 0.4$. Additionally, Ref.[16] noticed that the broad H$\alpha$ is well fitted by two Gaussian components, similarly to what we find, and used the whole profile of the two combined broad components to derive the BH mass. However, we have shown that the narrower broad component is actually extended and likely associated with a weak outflow. If we take only the broader Gaussian, together with the revised extinction, the inferred BH mass is $\log(M_{BH}/M_\odot) = 7.2$, which is what we have used in this paper.

### Dynamical mass

Ref.[16] estimated the dynamical mass in the central region by using the observed width of the narrow component of H$\alpha$ together with virial calibrations from Ref.[74] and Ref.[75], to derive $M_{dyn} = 10^{7.1} - 10^8$ $M_\odot$. They adopted an upper limit on the radius of 30 pc given by the higher resolution NIRCam imaging[14]. We have found that the narrow component of the Balmer lines has an extended component. However, within the central aperture the emission is dominated by a compact, unresolved component. Therefore, in the central region we keep the same estimate as Ref.[16] for the dynamical mass in the central region, by conservatively taking the upper value of $M_{dyn} = 10^8$ $M_\odot$.

For the dynamical mass in the outer annulus, when comparing with simulations one should still take the dynamical mass of the central region, which is where the stellar mass is contained (based on the unresolved images of the continuum emission). However, we conservatively take the dynamical mass estimated on the larger annulus. In this cases we take as the radius containing half of the narrow line emission, i.e. 200 pc. Adopting the same methodology as Ref.[16], this gives an outer dynamical mass of $M_{dyn} = 6\times10^8$ $M_\odot$.

### Ruling out high density scenario for the weakness of [OIII]

The lack of a broad component of [OIII]5007 is expected, as the gas density in the BLR ($n \sim 10^9 - 10^{12}$ cm$^{-3}$) is much higher than

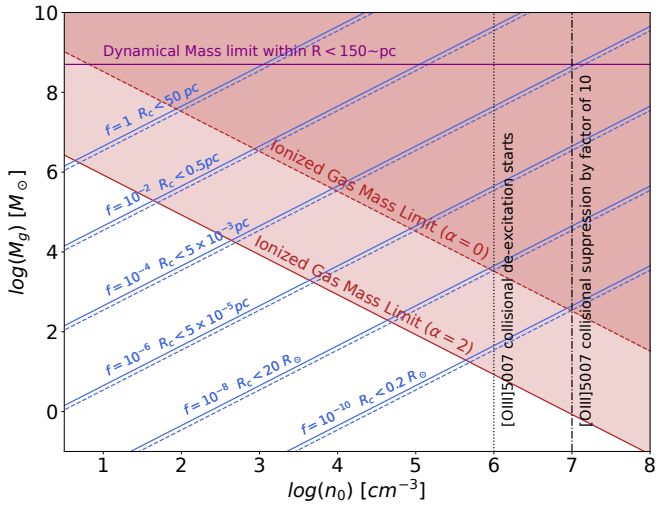


**Extended Data Fig. 5 |** Constraints on the gas density for the gas emitting the narrow emission lines. The blue lines indicate the gas mass enclosed within the central aperture for as a function of gas density $n_0$ at $R = 100pc$, for a power-law radial distribution $n \propto r^{-\alpha}$ with index $\alpha = 2$ (solid) and $\alpha = 0$ (dashed), for different filling factors (and implied upper limits on the clouds size) as indicated. The red lines indicate the mass of ionized gas constrained by the H$\beta_N$ luminosity for the two power indices. The vertical dotted line indicates the density where collisional de-excitation of [OIII]5007 starts to affect its flux by ~ 50%, the dot-dashed line it the density required to suppress the flux by a factor of 10. Explaining the weakness of [OIII]5007 via collisional de-excitation would require extremely low filling factors and clouds smaller than stars.

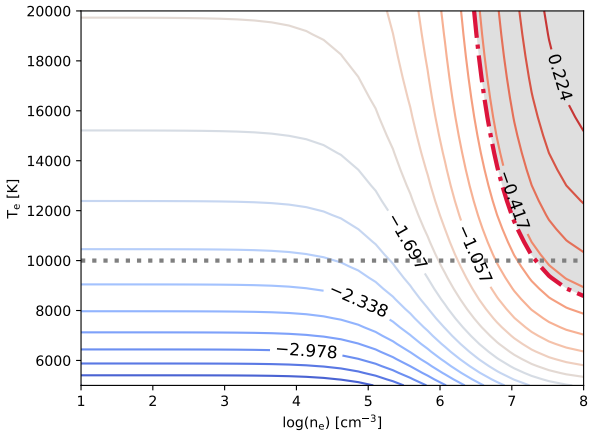


**Extended Data Fig. 6 |** [OIII]4363/[OIII]5007 flux ratio as a function of temperature and density. The observed upper limit [OIII]4363/[OIII]5007<0.33 is marked with a dot-dashed line and indicate densities $< 10^7\ cm^{-3}$ for reasonable temperatures $T > 10^4\ K$.

the critical density of this transition ($n_c = 7 \times 10^5$ cm$^{-3}$), hence this line is collisionally de-excited in the BLR, relative to H$\beta$. The weakness of [OIII]5007 relative to the *narrow* component of H$\beta$ is instead much more difficult to explain, and actually unphysical, in a high density scenario, as discussed in the following.

Although the densities of the ionized ISM are found, on average, to increase in high-z galaxies, they are still found to be below $< 10^5$ cm$^{-3}$ [76,77] (one case found to have $n > 10^6$ cm$^{-3}$ has actually ascribed to the BLR of an AGN, with $n \sim 10^{10}$ cm$^{-3}$)[37]. In any case, we can directly provide constraints on the density of the gas in the ionized gas of QSO1 that produces the narrow lines. We focus on the spectrum extracted from the central aperture ($R < 150$ pc); the arguments would be even stronger for the larger aperture. We assume a radial density distribution following a powerlaw

$$n(r) = n_0 \left(\frac{r}{r_0}\right)^{-\alpha}$$

where $n_0$ is the density at a reference radius $r_0$. We take $r_0 = 100$ pc, i.e. well within the aperture. We also assume that the clouds with such density have a filling factor $f$ defined as

$$f = \frac{V_{clouds}}{V_{tot}} = \frac{N_{clouds} R_c^3}{R_{max}^3}$$

where $V_R$ is the volume enclosed in the aperture, assumed spherical with radius $R_{max}$, $V_{clouds}$ is the volume occupied by the ionized clouds, and $N_{clouds}$ is the number of clouds and $R_c$ is their radius. The mass of gas contained within the aperture is given (assuming a medium made only of hydrogen for simplicity)

$$M_g = \int_{R_{min}}^{R_{max}} n(r)\, m_p\, f\, 4\pi r^2\, dr$$

where $m_p$ is the proton mass. For $R_{min}$ we take 5 pc, as smaller radii would make the line broader because they would be within the sphere of influence of the black hole; we however note that selecting even smaller inner radii would make the arguments even stronger. The blue lines in Extended Data Fig.5 show the implied gas mass as a function of density for different values of the filling factor $f$. We also indicate, for each filling factor, the implied maximum size of the clouds obtained by assuming the extreme case that all gas is contained in a single cloud ($N_{clouds} = 1$), while in reality the clouds would be much smaller. We then derive the mass of ionized gas inferred from the luminosity of $H\beta_N$

$$\frac{M_{ion}}{M_\odot} = 10^9 \frac{L(H\beta_N)}{10^{43} erg\ s^{-1}} \frac{100\ cm^{-3}}{n_0} \frac{3-2\alpha}{3-\alpha} r_0^{-3\alpha} \frac{R_{max}^{3-\alpha} - R_{min}^{3-\alpha}}{R_{max}^{3-2\alpha} - R_{min}^{3-2\alpha}}$$

We have assumed a temperature T=10,000 K, the results would be even tigther if assuming a higher temperature. The resulting constraint on the mass of ionized gas is shown with a red solid line in Fig.5, in the case of $\alpha = 2$. We also show the extreme (unlikely) case of $\alpha = 0$ (i.e. uniform distribution) with a red dashed line. In order for the gas to have a density higher than $10^6$ cm$^{-3}$, at which [OIII]5007 starts to be collisionally suppressed by a factor of 1.5 (which would still not affect significantly our results) the ionized clouds should have an extremely small filling factor ($f < 10^{-8} - 10^{-10}$) and should be smaller than stars. We have used Cloudy models to infer that, in order to suppress [OIII]5007 by a factor of ten, which would be needed to entirely ascribe to collisional de-excitation the lower [OIII]/H$\beta$ ratio relative to the other AGN and galaxies at z~7, the ISM would need to reach densities higher than $10^7$ cm$^{-3}$. As illustrated in Fig.5 (dot-dashed line) this would require even more extreme filling factors and clouds as small as planets.

Finally we note that the non detection of [OIII]4363, which has a critical densities much higher than [OIII]5007, also rules out high very high densities. Extended Data Fig.6 illustrates the variation of [OIII]4363/[OIII]5007 as a function of temperature and density, estimated with the Pyneb software[78]. For reasonable temperatures typical of the photoionized gas emitting H$\beta$ ($T > 10^4\ K$) the inferred upper limit in the central region ([OIII]4363/[OIII]5007<0.33, Tab.1) gives an upper limit on the density of $n < 10^7\ cm^{-3}$.

**Ruling out peculiar ionization scenarios for the [OIII] weakness**

In principle, another scenario to explain the weakness of [OIII] relative to H$\beta$, without invoking low metallicity and in the low density regime, is that the gas ionization state is so low that $O^{+2}$ is not produced. This would happen if the ionization parameter $U = Q_i/(4\pi r^2 nc)$ (where $Q_i$ is the rate of ionizing photons) is very low, much lower than typically observed in other galaxies. This would be in contrast with the finding that high-z galaxies are characterized by higher ionization parameters than lower redshift galaxies[60].

Additionally, a low ionization parameter would result in a relatively strong [OII]3727 emission, which is not detected. We have quantified the latter argument more in detail by using Cloudy photoionization modelling. We have inferred that (assuming an AGN SED), in the low density regime for the ISM ($n < 10^4$ cm$^{-3}$, which gives reasonable filling factors and cloud sizes, Extended Data Fig.5), the lower limit on $F([OIII]5007)/F([OII]3727) > 3$ (by also taking into accounting an extinction of $A_V = 0.66$) requires an ionization parameter log $U > -2.78$. With such a constraint on the ionization parameter it is not possible to reproduce the observed low [OIII]/H$\beta$ ratio with the typical metallicity observed in other high-z galaxies of $Z \sim 0.1\ Z_\odot$. Reproducing the observed [OIII]/H$\beta$ ratio, while maintaining log $U > -2.78$, requires lowering the metallicity, with an upper limit of $log(Z/Z_\odot) < -1.7$, i.e. close to the value inferred from the calibrations.

It is also possible to exclude a low ionization parameter solution based on simple geometrical arguments and based on the gas distribution. The source of UV radiation powering the narrow line (be it AGN or star formation) is unresolved, and confined within $r < 30$ pc[14]. For simplicity, and conservatively, we assume it to be point-like. From the H$\alpha$ luminosity (corrected for extinction) we infer a production of ionizing photons $Q_i = 1.4 \times 10^{54}$ s$^{-1}$. The surface brightness profile within the central aperture is not resolved. However, assuming, as in the previous section, a typical powerlaw density profile with power index $-2$, the luminosity weighted radius within the aperture is 77 pc. Conservatively assuming an upper limit on density of $n < 10^4$ cm$^{-3}$ we obtain a lower limit on the ionization parameter of log $U > -2.2$. With such a high value of the ionization parameter, suppressing [OIII] to the observed value of [OIII]/H$\beta$ would require a metallicity $Z < 10^{-1.9}\ Z\odot$.

A similar scenario for explaining the low [OIII]/H$\beta$ could be that, without invoking low metallicity, the ionizing spectrum is deficient in photons energetic enough to ionize $O^+$. However, this scenario would not explain the absence of [OII], as oxygen has about the same ionization potential as hydrogen. Similarly, [NII] and [SII] should be quite strong[79].

The opposite scenario would be that the ionization of the gas is so high that oxygen is mostly in $O^{+3}$. However, it has never been seen, not even in the most extreme AGN, that the ionization of the gas is so high to suppress [OIII] emission[80]. In any case, such a high level of ionization would result in other high ionization lines, such as CIV and HeII, to be very strong. In particular, using Cloudy modelling, we infer that in order to make [OIII]/H$\beta$ as faint as observed, while keeping the metallicity $lg(Z/Z_\odot) > -1.5$ and assuming an AGN ionizing spectrum, it would require an extremely high ionization parameter, higher than about unity. In such conditions HeII$\lambda$4686 should be about as strong as [OIII], or even stronger, while HeII is undetected.

**Semi-Analytical Models and Hydrodynamical Symulations**

In this section we provide additional information on the semi-analytical models and hydrodynamical simulations that have been used in Fig. 3.

**DELPHI**

Delphi (**D**ark Matter and the **e**mergence of ga**l**axies in the e**p**oc**h** of re**i**onization) is a semi-analytic model that uses a binary merger tree approach to jointly track the build-up of dark matter halos, their baryonic components (gas, stellar, dust and metal masses) and black holes at $z >= 4.5$[81–84] using the Planck 2020 cosmological model[46]. We follow the assembly of dark matter halos between $\log_{10}(M_{\rm h}/{\rm M}_\odot) = 8 - 14$ from $z \sim 40$ down to $z = 4.5$ with a mass resolution of $10^8$ M$_\odot$. Crucially, this model has been calibrated against the latest datasets for both star forming galaxies and black holes assimilated by the JWST and ALMA, and run exploring: (i) different seeding prescriptions including *light* (100M$_\odot$) and *heavy* seeds ($10^{3-5}$M$_\odot$); (ii) different spins exploring cases with spin values of $s = 0, +1, -1$; (iii) allowing black hole growth in both Eddington-limited and super-Eddington accretion scenarios. In this model, the growth of black holes is regulated both by the host halo mass and the gas mass left after star formation and the associated Type II Supernova (SNII) feedback. Our model includes a "critical" halo mass for efficient black hole accretion with a value that evolves with redshift as $M_{\rm bh}^{\rm crit}(z) = 10^{11.25}[\Omega_m(1+z)^3 + \Omega_\Lambda]^{-0.125}$ on which we include a scatter of 0.5 dex, motivated by the results of cosmological simulations[85]. In order to explain the number density of JWST-detected AGN, at any time-step black holes are allowed to accrete a gas mass of $M_{\rm bh}^{\rm crit}(z) = min[\epsilon_r f_{\rm bh}^{\rm ac} M_{\rm g}^{\rm sf}, f_{\rm Edd}\ m_{\rm Edd}]$ where $M_{\rm g}^{\rm sf}$ is the gas mass left after star formation and its associated SNII feedback, $f_{\rm Edd}$ is the Eddington fraction and $m_{\rm Edd}$ is the Eddington accretion rate. Allowing very weak AGN feedback (0.01% of black holes feedback coupling to the gas) we require values of $f_{\rm bh}^{\rm ac} = 0.1\ (5 \times 10^{-4})$ and $f_{\rm Edd} = 1.0\ (10^{-4})$ for halos above (below) the critical mass (we allow 0.5 dex of scatter on all of these quantities); i.e. black holess in high-mass (low-mass) halos can accrete the minimum between 10% (0.05%) of the available gas mass and 100% (0.01%) of the Eddington fraction. Assuming instantaneous recycling and perfect mixing of gas, dust and metals, we model the interlinked dust and metal contents of early systems including all of the relevant processes: for dust we account for production in SNII, destruction in SNII shocks, astration into star formation, ejection in outflows and grain growth in the cold inter-stellar medium. The time-evolution of metal enrichment is calculated as

$$\frac{dM_{\rm Z}}{dt} = \dot{M}_{\rm Z}^{\rm pro} - \dot{M}_{\rm Z}^{\rm ast} + \dot{M}_d^{\rm des} - \dot{M}_{\rm Z}^{\rm eje} - \dot{M}_d^{\rm gro}. \quad (1)$$

where the terms on the right hand side account for the rate of metal production ($\dot{M}_{\rm Z}^{\rm pro}$) including the latest state-of-the-art yields from Type Ia SN (SNIa), SNII and Asymptotic Giant branch (AGB) stars from[86], the rate of metals astrated into star formation ($\dot{M}_{\rm Z}^{\rm ast}$), the rate of dust mass destruction in SNIII shocks that adds to the metal content ($\dot{M}_d^{\rm des}$), the rate of metals lost in outflows ($\dot{M}_{\rm Z}^{\rm eje}$ ) and the rate of metals lost to dust grain growth in the cold ISM ($\dot{M}_d^{\rm gro}$). This model has already been used to study the contribution of black holes to the reionization process[?] and been pushed to its extreme limits to explain the enormous black hole-to-stellar mass ratios being observed with the JWST[14].

### CAT

The Cosmic Archaeology Tool[87,88] is a versatile semi-analytical model designed to trace and reproduce the early galaxy evolution during the first Gyr of cosmic history. Its primary goal is to explore how different formation and accretion scenarios for the first BH seeds contribute to the build-up of the massive BH population, as well as their co-evolution with host galaxies over cosmic time. CAT runs on a suite of semi-analytical dark matter merger trees, offering a large statistical sampling of the galaxy population from $z \approx 25$ down to $z = 4$. It resolves the formation of the first cosmic structures, with a minimum halo mass resolution of $\sim 10^6\,\mathrm{M}_\odot$, following the hierarchical assembly of dark matter halos up to $\log(\mathrm{M_h}/\mathrm{M}_\odot) = 14$. In each halo, CAT characterizes the formation of both PopIII and PopII stars, depending on the galaxy metallicity[89]. The code then self-consistently tracks the enrichment of the ISM with dust and metals from both SNe and AGB stars, relying on mass- and metallicity-dependent stellar yields. The model include a two-phase ISM, where dust grains can be destroyed by SN shocks in the diffuse hot medium or grow in mass by accreting gas-phase metals in warm, dense gas. Mechanical feedback from SN explosions and AGN accretion is also included, potentially driving energy-driven galaxy-scale winds[90]. The enrichment of IGM is evolved across different merger trees, consistently with the predicted galaxy outflows. It is worth noting though that, due to the lack of spatial information on the DM halo distribution (which is an intrinsic limitation of our semi-analytical merger trees) the IGM metallicity is modeled as an average quantity. This value evolves with redshift and depends on the simulated overdensity. In reality, the patchy IGM enrichment might translate in lower metallicity levels than those predicted by the model for systems evolving in relative isolation.

The BH formation is implemented following two different seeding channels: *light seeds* ($M_{\rm seed} \sim 100\,M_\odot$) form as remnants of PopIII stars, (formed in galaxies with metallicity below a critical threshold of $Z_{\rm crit} = 10^{-3.8}\,Z_\odot$). When the stellar population evolves, the most massive BH remnant formed is retained as the galaxy nuclear BH. *Heavy seeds* ($M_{\rm seed} = 10^5\,M_\odot$) are assumed to form instead through the so-called direct collapse scenario[91,92], under specific conditions for the host galaxy. The host halo must be metal-poor ($Z < Z_{\rm crit}$), support atomic hydrogen cooling ($T_{\rm vir} > 10^4$ K), and be exposed to a sufficiently strong Lyman-Werner radiation to suppress molecular hydrogen formation and prevent gas fragmentation, enabling the monolithic collapse of the gas. This last condition corresponds to a critical LW flux threshold of $J_{\rm LW} = 300\,J_{21}$, where $J_{21} = 10^{-21}\,\mathrm{erg\,s^{-1}\,cm^{-2}\,sr^{-1}\,Hz^{-1}}$.

The catalogues presented in this work consider two distinct accretion scenarios driving the subsequent BH growth[87]. In the Eddington-limited (EL) model, nuclear BHs grow at the Bondi rate[93], with accretion capped at the Eddington limit. Due to the strong dependence of the Bondi rate on BH mass, light seeds are unable to grow significantly in this scenario. As a result, the massive BH population at high redshift originates exclusively from heavy seed progenitors. In the super-Eddington (SE) model, on top of the Bondi accretion, we allow for short episodes of enhanced accretion during major galaxy mergers (with typical durations of $\Delta t \sim 1$ Myr[31]). These bursts are assumed to be driven by strong gas inflows into the nuclear region, triggered by angular momentum loss during mergers. During these phases, the BH accretion rate is modelled as $\dot{M}_{\rm BH} = \epsilon_{\rm BH} M_{\rm gas}/\tau_{\rm bulge}$, i.e. proportional to the galaxy gas content and independent of BH mass. These episodes of enhanced accretion are often characterized by super-Eddington rates, particularly for low-mass BHs, enabling light seeds to grow efficiently already at early times. Therefore, in this scenario, both light and heavy seeds contribute to the build-up of the massive BH population, with rapidly growing light seeds representing a competitive channel to the direct collapse scenario.

### AESOPICA

Aesopica is a new suite of large-volume cosmological simulations (Koudmani et al., in prep) built upon the Fable galaxy formation model[32]. The Fable sub-grid models are largely based on the Illustris galaxy formation model[94]. Whilst the models for star formation[95], radiative cooling[96,97], and chemical enrichment[98] are unchanged from Illustris, the stellar feedback[99] and AGN feedback[100] models have been updated to include thermal stellar feedback and an AGN duty cycle. Aesopica introduces additional targeted updates for modelling the growth of infant black holes in the early Universe, exploring three key modifications to fiducial galaxy formation models: enabling efficient accretion in the low-mass regime[33], incorporating super-Eddington accretion, and examining a broad range of seed masses ($10^2$ $\mathrm{M}_\odot$ to $10^5$ $\mathrm{M}_\odot$) following seed evolution from early cosmic epochs ($z \sim 20$). This is achieved by lowering the halo mass threshold for seeding black holes to the smallest resolvable halo size to $3\times10^9$ $\mathrm{M}_\odot$. We note that this represents a likely optimistic seeding scenario, so our black hole occupation for resolved haloes should be seen as an upper limit.

### Phanes: an analytic formalism for primordial black holes

We use the results obtained within the context of the phanes (**P**rimordial black **h**oles **a**ccelerating the assembly of **n**ascent **e**arly **s**tructures) analytic formalism. This is described in detail in Dayal et al. (2025, in prep.). This work follows the time-evolution of galaxies seeded by primordial black holes. It purely focuses on the "seed effect" where the Coulomb effect of a single black hole can generate an initial density fluctuation that grows through gravitational instability[101,12]. Black holes start accreting dark matter linearly starting at the redshift of matter-radiation equality ($z \sim 3400$) such that by $z \sim 34$, the dark matter halo starts dominating the potential. At this point, the halo is allowed to grow non-linearly using the accretion rate from state-of-the-art N-body simulations[102]. A halo is allowed to accrete gas - at a rate driven by the cosmological baryon-to-dark matter ratio - once its mass is sufficient to host a baryonic over-density of about 200. This gas can be accreted onto the black hole to allow its growth, and form stars. The phanes formalism also accounts for the feedback from both Type II Supernovae (SNII) and BH accretion in determining the final gas mass at the end of any time-step; this acts as the initial gas mass for the next time-step in order to track the baryonic assembly of such early systems. Assuming perfect mixing of metals and gas, the formalism accounts for the key processes of metal production (where the latest mass-dependent stellar yields from[86] are used), astration into black hole accretion and star formation, and loss in BH- and SNII-powered outflows in order to calculate the metal enrichment of these early systems.

### PBH hydrodynamical simulations

Using cosmological N-body and hydrodynamic simulations with the Gizmo code[103], we model the formation of the first galaxies in PBH-seeded halos, taking into account the accretion and feedback of an isolated PBH with $10^6\,M_\odot$. This PBH mass scale naturally arises from the thermal history of the ultra-early Universe, related to the

$e^+e^-$ phase transition. To simulate the formation of structure around the PBH, we adopt the numerical recipes summarized in ref. [34], to which we refer for further details. We specifically implement a star formation prescription for Jeans unstable gas in the vicinity of an accreting PBH, taking into account the intricate interaction between the different gaseous components.

The accretion-driven growth of the initial PBH is sensitive to the coupling strength of the accretion-generated luminosity, $L_{\rm BH}$, to the surrounding gas, modeled as thermal energy injection with $\delta E = \epsilon_r L_{\rm BH} \delta t$, given a simulation timestep $\delta t$. The maximal growth is realized for the limiting case of negligible thermal coupling $\epsilon_r \simeq 0$, establishing $M_{\rm BH} \simeq 10^7 M_\odot$ by $z \sim 9$, close to what is inferred for QSO1. The (radiation-hydrodynamical) gas flows in the vicinity of the accreting PBH, however, are complex, and follow-up simulations are required to determine the branching ratio of such large-scale inflows into feeding of the black hole and of the concurrent starburst, covering a statistically representative sample of environments.

We track the metallicity evolution in galaxies, incorporating both star formation and gas outflows driven by black hole feedback. The metallicity $Z$ of a galaxy at a given time $t$ is defined as the ratio of metal mass $M_Z(t)$ to gas mass $M_{\rm gas}(t)$, contained within the outflow bubble:

$$Z(t) = \frac{M_Z(t)}{M_{\rm gas}(t)} \,, \tag{2}$$

assuming a uniform distribution within this bubble and ignoring metal diffusion at the bubble surface.

The metal mass is given by

$$M_Z(t) = \mathcal{M}_Z M_{\rm star}(t) \,, \tag{3}$$

where $M_{\rm star}(t)$ is the stellar mass, and $\mathcal{M}_Z$ is the metal yield per unit stellar mass, which depends on the stellar initial mass function (IMF) and stellar evolution models for winds and supernovae. Based on the stellar evolution models in ref. [45], we estimate $\mathcal{M}_Z$ to be in the range $\sim 0.02 - 0.19$, bracketing the plausible range for different IMFs (from present-day to Pop III stars).

We estimate the size of the outflow bubble as the radius where the average outflow velocity drops below the local sound speed, and further simplify our model by neglecting the delay between star formation and subsequent metal enrichment due to stellar evolution. Fig. 3d shows representative trajectories for the resulting metallicity evolution, where each line corresponds to a simulation run with different initial conditions. We again refer to ref. [34] for a detailed description of the numerical implementation and simulation parameters.

We conclude the discussion on the PBHs scenarios by mentioning that this class of models had many more observational predictions to be tested, especially in terms of luminosity and mass of the stellar component [104], which may be tested with future observations.

## References (continued)


46. Planck Collaboration et al., 2020. Planck 2018 results. VI. Cosmological parameters, A&A, 641, A6
47. D'Eugenio F., et al., 2024. JADES Data Release 3 – NIRSpec/MSA spectroscopy for 4,000 galaxies in the GOODS fields, p. arXiv:2404.06531 arXiv:2404.06531
48. Jakobsen P., et al., 2022. The Near-Infrared Spectrograph (NIRSpec) on the James Webb Space Telescope. I. Overview of the instrument and its capabilities, A&A, 661, A80
49. Böker T., et al., 2023. In-orbit Performance of the Near-infrared Spectrograph NIRSpec on the James Webb Space Telescope, PASP, 135, 038001
50. Konstantopoulou C., et al., 2024. Dust depletion of metals from local to distant galaxies. II. Cosmic dust-to-metal ratio and dust composition, A&A, 681, A64
51. Zhu H., Tian W., Li A., Zhang M., 2017. The gas-to-extinction ratio and the gas distribution in the Galaxy, MNRAS, 471, 3494
52. Harikane Y., et al., 2025. Its Impact on Metallicity Measurements, p. arXiv:2505.09186 arXiv:2505.09186
53. Scholtz J., et al., 2025. Tentative rotation in a galaxy at z∼14 with ALMA, p. arXiv:2503.10751 arXiv:2503.10751
54. Witstok J., et al., 2022. Dual constraints with ALMA: new [O III] 88-$\mu$m and dust-continuum observations reveal the ISM conditions of luminous LBGs at z 7, MNRAS, 515, 1751
55. Curti M., Mannucci F., Cresci G., Maiolino R., 2020. The mass-metallicity and the fundamental metallicity relation revisited on a fully $T_e$-based abundance scale for galaxies, MNRAS, 491, 944
56. Baldwin J. A., Phillips M. M., Terlevich R., 1981. Classification parameters for the emission-line spectra of extragalactic objects., PASP, 93, 5
57. Veilleux S., Osterbrock D. E., 1987. Spectral Classification of Emission-Line Galaxies, ApJS, 63, 295
58. Kewley L. J., Heisler C. A., Dopita M. A., Lumsden S., 2001. Optical Classification of Southern Warm Infrared Galaxies, ApJS, 132, 37
59. Kauffmann G., et al., 2003. The host galaxies of active galactic nuclei, Monthly Notices of the Royal Astronomical Society, 346, 1055
60. Cameron A. J., et al., 2024. Nebular dominated galaxies: insights into the stellar initial mass function at high redshift, MNRAS, 534, 523
61. Strom A. L., et al., 2017. Nebular Emission Line Ratios in z = 2-3 Star-forming Galaxies with KBSS-MOSFIRE: Exploring the Impact of Ionization, Excitation, and Nitrogen-to-Oxygen Ratio, ApJ, 836, 164
62. Lambrides E., et al., 2024. The Case for Super-Eddington Accretion: Connecting Weak X-ray and UV Line Emission in JWST Broad-Line AGN During the First Gyr of Cosmic Time, p. arXiv:2409.13047 arXiv:2409.13047
63. Scholtz J., et al., 2023. JADES: A large population of obscured, narrow line AGN at high redshift, p. arXiv:2311.18731 arXiv:2311.18731
64. Mazzolari G., et al., 2024. Narrow line AGN selection in CEERS: spectroscopic selection, physical properties, X-ray and radio analysis, p. arXiv:2408.15615 arXiv:2408.15615
65. Übler H., et al., 2023. GA-NIFS: A massive black hole in a low-metallicity AGN at z ∼ 5.55 revealed by JWST/NIRSpec IFS, A&A, 677, A145
66. Dalla Bontà E., et al., 2025. Estimating masses of supermassive black holes in active galactic nuclei from the H$\alpha$ emission line, A&A, 696, A48
67. Lupi A., Quadri G., Volonteri M., Colpi M., Regan J. A., 2023. Sustained super-Eddington accretion in high-redshift quasars, p. arXiv:2312.08422 arXiv:2312.08422
68. Marconi A., et al., 2008. The Effect of Radiation Pressure on Virial Black Hole Mass Estimates and the Case of Narrow-Line Seyfert 1 Galaxies, ApJ, 678, 693
69. Marconi A., et al., 2009. On the Observed Distributions of Black Hole Masses and Eddington Ratios from Radiation Pressure Corrected Virial Indicators, ApJ, 698, L103

70. Abuter R., et al., 2024. A dynamical measure of the black hole mass in a quasar 11 billion years ago, p. arXiv:2401.14567 arXiv:2401.14567
71. Rusakov V., et al., 2025. JWST's little red dots: an emerging population of young, low-mass AGN cocooned in dense ionized gas, p. arXiv:2503.16595 arXiv:2503.16595
72. Cracco V., et al., 2016. A spectroscopic analysis of a sample of narrow-line Seyfert 1 galaxies selected from the Sloan Digital Sky Survey, MNRAS, 462, 1256
73. Du P., Wang J.-M., 2019. The Radius-Luminosity Relationship Depends on Optical Spectra in Active Galactic Nuclei, ApJ, 886, 42
74. van der Wel A., et al., 2022. The Mass Scale of High-redshift Galaxies: Virial Mass Estimates Calibrated with Stellar Dynamical Models from LEGA-C, ApJ, 936, 9
75. Stott J. P., et al., 2016. The KMOS Redshift One Spectroscopic Survey (KROSS): dynamical properties, gas and dark matter fractions of typical z ∼ 1 star-forming galaxies, MNRAS, 457, 1888
76. Isobe Y., et al., 2023. Redshift Evolution of Electron Density in the Interstellar Medium at z 0-9 Uncovered with JWST/NIRSpec Spectra and Line-spread Function Determinations, ApJ, 956, 139
77. Topping M. W., et al., 2025. Deep Rest-UV JWST/NIRSpec Spectroscopy of Early Galaxies: The Demographics of C IV and N-emitters in the Reionization Era, ApJ, 980, 225
78. Luridiana V., Morisset C., Shaw R. A., 2015. PyNeb: a new tool for analyzing emission lines. I. Code description and validation of results, A&A, 573, A42
79. Rhea C. L., et al., 2025. Mapping the Filamentary Nebula of NGC 1275 with Multiwavelength SITELLE Observations, AJ, 169, 203
80. Dors O. L., et al., 2020. Chemical abundances of Seyfert 2 AGNs - III. Reducing the oxygen abundance discrepancy, MNRAS, 496, 3209
81. Dayal P., Ferrara A., Dunlop J. S., Pacucci F., 2014. Essential physics of early galaxy formation, MNRAS, 445, 2545
82. Dayal P., et al., 2019. The hierarchical assembly of galaxies and black holes in the first billion years: predictions for the era of gravitational wave astronomy, MNRAS, 486, 2336
83. Piana O., Dayal P., Choudhury T. R., 2022. The impact of black hole feedback on the UV luminosity and stellar mass assembly of high-redshift galaxies, MNRAS, 510, 5661
84. Dayal P., et al., 2025. UNCOVERing the contribution of black holes to reionization, A&A, 697, A211
85. Bower R. G., et al., 2017. The dark nemesis of galaxy formation: why hot haloes trigger black hole growth and bring star formation to an end, MNRAS, 465, 32
86. Kobayashi C., Karakas A. I., Lugaro M., 2020. The Origin of Elements from Carbon to Uranium, ApJ, 900, 179
87. Trinca A., et al., 2022. The low-end of the black hole mass function at cosmic dawn, MNRAS, 511, 616
88. Trinca A., et al., 2023. Seeking the growth of the first black hole seeds with JWST, MNRAS, 519, 4753
89. Trinca A., et al., 2024. Exploring the nature of UV-bright z ≳ 10 galaxies detected by JWST: star formation, black hole accretion, or a non-universal IMF?, MNRAS, 529, 3563
90. Valiante R., Schneider R., Volonteri M., Omukai K., 2016. From the first stars to the first black holes, Monthly Notices of the Royal Astronomical Society, 457, 3356
91. Bromm V., Loeb A., 2003. Formation of the First Supermassive Black Holes, ApJ, 596, 34
92. Begelman M. C., Volonteri M., Rees M. J., 2006. Formation of supermassive black holes by direct collapse in pre-galactic haloes, MNRAS, 370, 289
93. Bondi H., 1952. On spherically symmetrical accretion, MNRAS, 112, 195
94. Vogelsberger M., et al., 2014. Introducing the Illustris Project: simulating the coevolution of dark and visible matter in the Universe, MNRAS, 444, 1518
95. Springel V., Hernquist L., 2003. Cosmological smoothed particle hydrodynamics simulations: a hybrid multiphase model for star formation, MNRAS, 339, 289
96. Katz N., Weinberg D. H., Hernquist L., 1996. Cosmological Simulations with TreeSPH, ApJS, 105, 19
97. Wiersma R. P., Schaye J., Smith B. D., 2009a. The effect of photoionization on the cooling rates of enriched, astrophysical plasmas, MNRAS, 393, 99
98. Wiersma R. P., Schaye J., Theuns T., Dalla Vecchia C., Tornatore L., 2009b. Chemical enrichment in cosmological, smoothed particle hydrodynamics simulations, MNRAS, 399, 574
99. Vogelsberger M., et al., 2013. A model for cosmological simulations of galaxy formation physics, MNRAS, 436, 3031
100. Sijacki D., et al., 2015. The Illustris simulation: The evolving population of black holes across cosmic time, MNRAS, 452, 575
101. Carr B., Silk J., 2018. Primordial black holes as generators of cosmic structures, MNRAS, 478, 3756
102. Trac H., Cen R., Mansfield P., 2015. SCORCH I: The Galaxy-Halo Connection in the First Billion Years, ApJ, 813, 54
103. Hopkins P. F., 2015. A new class of accurate, mesh-free hydrodynamic simulation methods, MNRAS, 450, 53
104. Matteri A., Pallottini A., Ferrara A., 2025. Can primordial black holes explain the overabundance of bright super-early galaxies?, A&A, 697, A65

## Acknowledgements

We thank Andrea Ferrara for useful suggestions. This work is based on observations made with the National Aeronautics and Space Administration (NASA)/European Space Agency (ESA)/Canadian Space Agency (CSA) JWST. The data were obtained from the Mikulski Archive for Space Telescopes at the STScI, which is operated by the Association of Universities for Research in Astronomy, Inc., under NASA contract NAS 5-03127 for JWST. These observations are associated with programme PID 5015. RM, FD, JS, IJ, GJ acknowledge support from the Science and Technology Facilities Council (STFC), by the European Research Council (ERC) through Advanced Grant 695671 "QUENCH", by the UK Research and Innovation (UKRI) Frontier Research grant RISEandFALL. RM also acknowledges support from a Royal Society Research Professorship grant. SZ, VB and BL acknowledge the Texas Advanced Computing Center (TACC) for providing HPC resources under allocation AST23026. GV acknowledges support by European Union's HE ERC Starting Grant No. 101040227 - WINGS. HÜ acknowledges funding by the European Union (ERC APEX, 101164796). Views and opinions expressed are however those of the authors only and do not necessarily reflect those of the European Union or the European Research Council Executive Agency. Neither the European Union nor the granting authority can be held responsible for them. K.I. acknowledges support from the National Natural Science Foundation of China (12233001), the National Key R&D Program of China (2022YFF0503401), and the China Manned Space Program (CMS-CSST-2025-A09).

## Author information


### Affiliations

[1]Kavli Institute for Cosmology, University of Cambridge, Madingley Road, Cambridge CB3 0HA, UK
[2]Cavendish Laboratory, University of Cambridge, 19 JJ Thomson Avenue, Cambridge CB3 0HE, UK
[3]Department of Physics and Astronomy, University College London, Gower Street, London WC1E 6BT, UK
[4]Max-Planck-Institut für extraterrestrische Physik, Gießenbachstraße 1, 85748 Garching, Germany
[5]Centro de Astrobiología (CAB), CSIC–INTA, Cra. de Ajalvir Km. 4, 28850- Torrejón de Ardoz, Madrid, Spain
[6]Department of Astronomy, University of Texas at Austin, Austin, TX 78712, USA
[7]Weinberg Institute for Theoretical Physics, Texas Center for Cosmology and Astroparticle Physics, University of Texas at Austin, Austin, TX 78712, USA
[8]Kapteyn Astronomical Institute, University of Groningen, PO Box 800, 9700 AV Groningen, The Netherlands
[9]St Catharine's College, University of Cambridge, Trumpington Street, Cambridge CB2 1RL, UK
[10]Institute of Astronomy, University of Cambridge, Madingley Road, Cambridge, CB3 0HA, UK
[11]Center for Computational Astrophysics, Flatiron Institute, 162 Fifth Avenue, New York, NY 10010, USA
[12]Centre for Astrophysics Research, Department of Physics, Astronomy and Mathematics, University of Hertfordshire, College Lane, Hatfield, AL10 9AB, UK
[13] Universität Heidelberg, Zentrum für Astronomie, Institut für Theoretische Astrophysik, D-69120 Heidelberg, Germany
[14]Dipartimento di Fisica, 'Sapienza' Università di Roma, Piazzale Aldo Moro 2, I-00185 Roma, Italy
[15]INAF/Osservatorio Astronomico di Roma, Via di Frascati 33, I-00040 Monte Porzio Catone, Italy
[16]INFN, Sezione Roma1, Dipartimento di Fisica, 'Sapienza' Università di Roma, Piazzale Aldo Moro 2, I-00185 Roma, Italy
[17]Sapienza School for Advanced Studies, Viale Regina Elena 291, I-00161 Roma, Italy
[18] Como Lake Center for Astrophysics, DiSAT, Università degli Studi dell'Insubria, via Valleggio 11, 22100, Como, Italy
[19]Department of Physics, University of Texas at Austin, Austin, TX 78712, USA
[20]Sorbonne Université, CNRS, UMR 7095, Institut d'Astrophysique de Paris, 98 bis bd Arago, 75014 Paris, France
[21]Kavli Institute for Astronomy and Astrophysics, Peking University, Beijing 100871, China
[22]Scuola Normale Superiore, Piazza dei Cavalieri 7, I-56126 Pisa, Italy
[23]Institute of Liberal Arts and Science Kanazawa University Kakuma Kanazawa, Ishikawa 920-1192, JAPAN
[24]Waseda Research Institute for Science and Engineering, Faculty of Science and Engineering, Waseda University, 3-4-1, Okubo, Shinjuku, Tokyo 169-8555, Japan
[25]Cosmic Dawn Center (DAWN), Copenhagen, Denmark
[26]Niels Bohr Institute, University of Copenhagen, Jagtvej 128, DK-2200, Copenhagen, Denmark
[27]Department of Physics, University of Oxford, Denys Wilkinson Building, Keble Road, Oxford OX1 3RH, UK
[28]European Southern Observatory, Karl-Schwarzschild-Strasse 2, 85748 Garching, Germany
[29] Università di Firenze, Dipartimento di Fisica e Astronomia, via G. Sansone 1, 50019 Sesto Fiorentino, Florence, Italy 2
[30]INAF – Arcetri Astrophysical Observatory, Largo E. Fermi 5, I50125, Florence, Italy
[31]Department of Astronomy & Astrophysics, University of Chicago, 5640 S Ellis Avenue, Chicago, IL 60637, USA
[32]Kavli Institute for Cosmological Physics, University of Chicago, Chicago IL 60637, USA
[33]AURA for European Space Agency, Space Telescope Science Institute, 3700 San Martin Drive. Baltimore, MD 21210, USA
[34]Aix Marseille Université, CNRS, CNES, LAM (Laboratoire d'Astrophysique de Marseille), UMR 7326, F-13388 Marseille, France
[35]Department of Astronomy and Astrophysics, University of California, Santa Cruz, 1156 High Street, Santa Cruz, CA 96054, USA
[36]Center for Astrophysics | Harvard & Smithsonian, 60 Garden St., Cambridge MA 02138, USA


### Author contributions

RM led the data analysis and the writing of this paper, with key contributions on these aspects from HÜ, FDE, JS, IJ. HÜ also led the preparation of the observations. HÜ, MP and FDE performed the data processing. VB, PD, SK, BL, RS, DS, RS, AT, SZ, MV, KI contributed to the development of the theoretical models, cosmological simulations and their comparison with the observations. YI and KN contributed with the development of photoionization models. EC and MC contributed with the development of the metallicity calibrations at high-z. SC, JW, GCJ, ST, SA, AB, SC, GC, ACF, NK, NL, MP, BR, FS and GV contributed to the interpretation of the results and to the assessment of different scenarios, and also provided comments on the manuscript.


### Correspondence

Correspondence should be addressed to R. Maiolino.


## Ethics declarations

### Competing interests

The authors declare no competing interests.

## References (continued)